Journal of The Electrochemical Society, 2020 **167** 110519

Physical Model and Machine Learning Enabled Electrolyte Channel Design for Fast Charging

Tianhan Gao[1] **and Wei Lu**[1,2,z]

[1]*Department of Mechanical Engineering, University of Michigan, Ann Arbor, Michigan 48109, United States of America*
[2]*Department of Materials Science and Engineering, University of Michigan, Ann Arbor, Michigan 48109, United States of America*

Thick electrode is highly effective to increase the specific energy of a battery cell, but the associated increase in transport distance causes a major barrier for fast charging. We introduce a bio-inspired electrolyte channel design into thick electrodes to improve the cell performance, especially under fast charging conditions. The effects of channel length, width, tapering degree and active material width on the electrochemical performance and mechanical integrity are investigated. Machine learning by deep neural network (DNN) is developed to relate the geometrical parameters of channels to the overall cell performance. Integrating machine learning with the Markov chain Monte Carlo gradient descent optimization, we demonstrate that the complicated multivariable channel geometry optimization problem can be efficiently solved. The results show that within a certain range of geometrical parameters, the specific energy, specific capacity and specific power can be greatly improved. At the same time, the maximum first principal stress which is in the cathode region next to the separator can be significantly reduced, giving better mechanical integrity. Comparing to conventional-designed cells without electrolyte channels, we show a 79% increase in specific energy using channel design optimization. This study provides a design strategy and optimization method to achieve significantly improved battery performance.
 [DOI: 10.1149/1945-7111/aba096]

Manuscript submitted March 29, 2020; revised manuscript received May 26, 2020. Published July 8, 2020.

List of symbols

Roman symbols

a_s	Active surface area per unit electrode volume (m^{-1})
A	Cross-sectional area of the electrode (m^2)
c_e	Lithium ion concentration in electrolyte (mol m^{-3})
c_s	Lithium concentration in solid (mol m^{-3})
c_{s0}	Initial lithium concentration in solid (mol m^{-3})
$c_{s,ave}$	Average lithium concentration in solid (mol m^{-3})
$c_{s,surf}$	Lithium concentration at particle surface (mol m^{-3})
$c_{s,max}$	Maximum lithium concentration in solid (mol m^{-3})
D_{e0}	Diffusivity of lithium ion in bulk electrolyte (m^2 s^{-1})
D_e^{eff}	Effective diffusivity of lithium ion in electrolyte phase (m^2 s^{-1})
D_s	Diffusivity of lithium ion in solid (m^2 s^{-1})
e	Eigenstrain of lithium intercalation
e_{ij}	Electrode level strain
E	Effective Young's modulus of the porous electrode (GPa)
E_{eq}	Equivalent potential (V)
E_p	Young's modulus of the solid particle (GPa)
$f_{\pm}$	Electrolyte active coefficient
F	Faraday's constant (C mol^{-1})
i	Reaction current density as the surface of the particle (A m^{-2})
i_0	Exchange current density at the surface of the particle (A m^{-2})
i_{app}	Applied charging or discharging current density (A m^{-2})
I	Discharging current (A)
k	Reaction rate constant ($m^{2.5}$ $mol^{-0.5}$ s^{-1})
L_n, L_p	Current collector thickness for the anode and cathode (μm)
L_{EA}, L_{EC}	Length of the channel in anode and cathode (μm)
L_s	Separator thickness (μm)
m	Mass of the full cell (kg)
m_{Al}	Aluminum current collector mass (kg)
m_{Cu}	Copper current collector mass (kg)
m_n	Anode mass (kg)
m_p	Cathode mass (kg)
m_{sep}	Separator mass (kg)
r	Radial coordinate (μm)
r_p	Particle radius (μm)
R	Ideal gas constant (J mol^{-1} K^{-1})
t	Time (s)
t_{ds}	Battery discharging start time (s)
t_{de}	Battery discharging end time (s)
t_+	Lithium ion transference number
T	Temperature (K)
u_i	Displacement (μm)
V_{mater}	Volume of electrode in anode or cathode (m^3)
$V_{channel}$	Volume of electrolyte channel in anode or cathode (m^3)
V_t	Terminal voltage (V)
W_{EA}, W_{EC}	Root width for the channel in anode and cathode (μm)
$W_{EA\text{-}b}$, $W_{EC\text{-}b}$	Tip width for the channel in anode and cathode (μm)
W_H	Periodic width (μm)
x, y	Coordinate (μm)

Greek symbols

α	Anodic charge transfer coefficient
ε_b	Electrode binding material volume fraction
ε_e	Electrolyte volume fraction
ε_s	Solid phase volume fraction
ε_{sep}	Separator solid phase volume fraction
ε	Sensitive factor
η	Over-potential (V)
κ_{e0}	Bulk electrolyte conductivity (S m^{-1})
κ_e^{eff}	Effective electrolyte phase conductivity (S m^{-1})
μ	learning rate
ν	Effective Possion's ratio for porous electrode
ν_p	Poisson's ratio of the solid particle
ρ	Density (kg m^{-3})
ρ_{Al}	Aluminum current collector density (kg m^{-3})
ρ_b	Electrode binding material density (kg m^{-3})
ρ_{Cu}	Copper current collector density (kg m^{-3})
ρ_e	Electrolyte density (kg m^{-3})
ρ_{Grap}	Anode active material density (kg m^{-3})

[z]E-mail: weilu@umich.edu

ρ_{LMO}	Cathode active material density (kg m^{-3})
ρ_{sep}	Separator material density (kg m^{-3})
σ_{s0}	Solid electronic conductivity (S m^{-1})
σ_s^{eff}	Effective solid phase conductivity (S m^{-1})
σ_h	Hydrostatic stress (MPa)
Σ_{ij}	Electrode level stress (MPa)
Φ_e	Electrolyte potential (V)
Φ_s	Solid potential (V)
Ω	Lithium ion partial molar volume (m^3 mol^{-1})

The lithium-ion battery (LIB) is widely used in many applications from consumer electronics to electric vehicles.[1,2] LIBs with thick electrode design have grained a lot of attention recently, where the increase in the volume fraction of active material comparing to current collector and other non-active components can effectively improve the specific energy and energy density. However, the thick electrode also increases the transport distance of ions and electrons.[3] As a result, the capacity utilization of active materials is reduced due to the associated polarization. The negative impact arising from longer diffusion distance is particularly significant under high current or fast charging conditions, while fast charging is increasingly demanded by many applications. In fact, the usable specific energy will decrease when the electrode is thicker than a threshold for any given current density requirement. Therefore, improving capacity utilization and rate performance for thick electrodes becomes highly important.

Several particle-level electrode designs have been proposed to increase the LIB performance, such as creating distributed porosity along the electrode thickness direction,[4] or aligning decorated graphite particles with magnetic field to reduce the diffusion tortuosity.[5] Besides, 3D electrodes have been explored for better performance, such as corrugating the current collectors, electrodes and separator together to form a trench architecture,[6–8] or forming the electrode into pillars arranged in interdigitated patterns.[9,10] These design strategies can reduce the ion diffusion distance and increase the contact area between the active material and the electrolyte. As a result, the battery performance in terms of energy, capacity or power density is improved. However, these kinds of strategies often require significant changes of the battery structure from the conventional configuration.

Introducing some forms of internal electrode-level architectures into the 2D planar electrode to increase its effective porosity is another way to improve the battery performance, which has been receiving increasing attention currently.[10–14] These architectures can further be used to affect tortuosity (quantification of ion conduction rate through the electrolyte of porous electrodes[15,16]). Besides, adding internal architectures into a planar electrode does not change the conventional sandwich battery structure, and there are many ways to manufacture architectures such as channels in an electrode. A channel design is much easier to be commercialized than complicated 3D structures.[17] The improvement in performance of electrodes containing architectures has been observed in several studies. Clancy et al.[18] numerically investigated the behavior of a Li-ion micro-battery with a core-shell structure so that the cathode rod (core) is surrounded by electrolyte (shell) on the side. By considering various types of electrolytes including solid-state, polymer, polymer-gel and liquid, they found overall improvement of battery capacity for all the electrolytes used as a result of the geometric effect of the structure. Ye et al.[17] considered a pore-network structure in the anode. The discharge energy density was calculated for selected structural parameters, electrode thickness, porosity and discharging C rate, showing that the performance improvement was dependent on the structural parameters. Reale et al.[19] added macroscopic pores into the electrode to reduce the effective tortuosity, and showed that the areal capacitance could be significantly improved. They also suggested that a bi-tortuous electrode design could be helpful for fast charging/discharging. Li et al.[20] brought grooves to the cathode and derived an analytical expression to estimate the improvement in specific capacity.

These studies suggest that introducing internal electrode-level architectures to the electrode can improve the performance without any change in the electrode material or the form factor of the electrode. The first aim of this paper is to systematically study the effect of adding tapered electrolyte channels in electrodes, quantifying both the electrochemical performance and mechanical integrity of the channel design during fast charging. The tapered channel design allows investigating a wide range of geometrical parameters not studied before, which will help understand the potential of performance improvement brought by electrolyte channels.

Electrochemical models[21–24] can be used to calculate the battery characteristics for any given sets of channel geometry by numerical approaches such as the finite element method (FEM). However, conducting parametric optimization using FEM is challenging due to the huge computational cost associated with the highly non-linear electrochemical model.[25] It is critical to find a method to effectively connect the geometrical parameters of an electrolyte channel to the battery cell performance, to be able to effectively conduct a parametric optimal design. The second aim of this paper is to introduce machine learning for channel design optimization.

Machine learning is gaining increasing attention in solving emerging problems, which can calculate the output with high efficiency after proper training. This approach overcomes the difficulties and computational cost of solving complex differential equations. Artificial neural network (ANN), an important machine learning technique, has been used to estimate the state of charge (SOC). Dang et al.[26] employed a dual network setup, with the first network to identify the electrochemical model parameters and the second one to capture the relationship between the open circuit voltage and SOC. Weigert et al.[27] applied ANN to predict the SOC for both battery and battery-supercapacitor systems. For LIB performance, Wu et al.[25] developed an ANN system that can automatically generate electrode design maps for any given specific energy and specific power requirement, providing design parameters such as electrode thickness and porosity. Their work highlighted that ANN can handle the non-linear, complex and computationally expensive problem of battery design and optimization. Takagishi et al.[28] utilized ANN to predict the charging and discharging resistance based on process parameters including active material porosity, particle radius, electrolyte conductivity, compacting pressure and binder/additive volume ratio. The predicted resistance by the ANN regression model matched well the simulation results. Parthiban et al.[29] demonstrated ANN to estimate and predict the specific capacity change of a LIB with a CoO anode for 50 cycles. These studies demonstrated the capability and accuracy of ANN in capturing complex, non-linear physical relationships. Here we develop ANN to perform analysis and design optimization of electrolyte channels.

In this paper we introduce a bio-inspired electrolyte channel design into thick electrodes to improve the battery performance during fast charging. The effects of channel length, width, tapering degree and width of active material on electrochemical performance and mechanical integrity are investigated by finite element simulations. These results provide a fundamental understanding of how the electrolyte channel parameters affect the battery performance, the local state of charge and the stress level of the active material. With the simulation results as the training data, a deep neural network (DNN) is developed to directly relate the electrolyte channel parameters to the specific energy, specific capacity and specific power. A Markov chain Monte Carlo method is used together with DNN to find the Ragone planes and the optimized channel designs. For the purpose of this study, we only consider the electrochemical performance in terms of specific energy, specific capacity and specific power. Side reactions such as lithium plating or cell degradation are not considered.

Modelling

Electrode with channels.—We first present a full cell model with bio-inspired channels in both the anode and cathode, as shown in

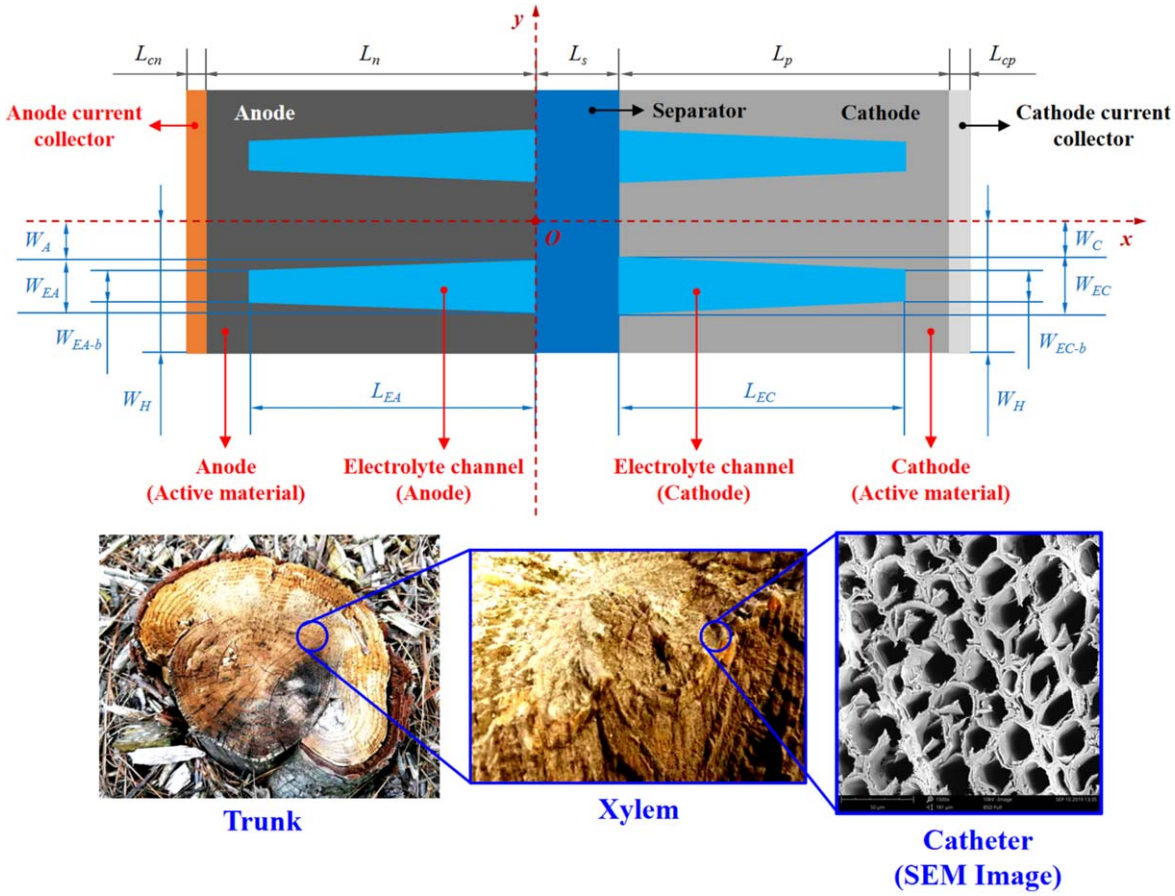

Figure 1. (Top) A full battery cell and the geometrical parameters of electrolyte channels. (Bottom) Our electrolyte channel design is motivated by the catheter structure in the xylem of a trunk, which facilities nutrition transport.

Fig. 1. The channel is filled with electrolyte. The geometry of a channel is characterized by its length (L_{EA} and L_{EC}, with subscript "A" denoting the anode channel and "C" denoting the cathode channel), root width (W_{EA} and W_{EC}) and tip width ($W_{EA\text{-}b}$ and $W_{EC\text{-}b}$). The half-widths of active electrode material between two neighboring channels at their roots are W_A and W_C. The structure is periodic along the in-plane direction (y-axis) of the electrode, and the periodic width is denoted by $W_H = W_{EA} + 2W_A = W_{EC} + 2W_C$. In this study, the anode thickness L_n and cathode thickness L_p are fixed as 250 μm. The separator has a thickness of $L_s = 30$ μm. The thickness of current collector for the anode (L_{cn}) and for the cathode (L_{cp}) are both 15 μm. For demonstration, here we use a graphite (Li_xC_6) anode and a $Li_yMn_2O_4$ (LMO) cathode. The current collector on the anode side is copper while on the cathode side is aluminum. The electrolyte is 1 M $LiPF_6$ in EC:DEC (1:1 wt%). It should be noted that while the channels appear aligned in Fig. 1, the result of this paper is applicable when the channels are not aligned. As shown later, the separator region will homogenize any y-axis variation of lithium ion concentration in the electrolyte, so that the lithium ion concentration is only a function of x before the ions reach the other electrode. In other words, the anode interacts with the separator region and then the separator region interacts with the cathode. The anode and cathode do not interact with each other directly. In practical applications, the channels of the two electrodes do not need to be aligned to benefit from the channel design.

The cell performance with the electrolyte channel design will be compared to that with the conventional electrode design having no channel. Our electrolyte channel design is motivated by the catheter structure in the xylem of a trunk (Fig. 1, bottom figure). With the catheter, nutrition can be easily transported from the root to the tree crown. Our hypothesis is that electrolyte channels in the electrodes can facilitate lithium ion transport in a similar way to improve the cell performance with thick electrodes during fast charging.

Electrochemical and mechanical modeling.— *Governing equations.*—We developed a pseudo three-dimensional electrochemical model and implemented it using COMSOL Multiphysics 5.4. The two electrode-level dimensions, as shown in Fig. 1, are the x-axis along the electrode thickness direction and the y-axis along the in-plane direction of the electrode. The third dimension is the r-axis along the radial direction of the active material particles.

The solid phase potential, Φ_s, and electrolyte phase potential, Φ_e, are given by

$$\nabla \cdot (\sigma_s^{eff} \nabla \Phi_s) = a_s i, \qquad [1]$$

$$\nabla \cdot \left\{ -\kappa_e^{eff} \left[\nabla \Phi_e - \frac{2RT}{F} \left(1 + \frac{d \ln f_{\pm}}{d \ln c_e} \right) (1 - t_+) \nabla \ln c_e \right] \right\} = a_s i, \qquad [2]$$

where the effective solid phase and electrolyte phase conductivities are given by $\sigma_s^{eff} = \sigma_{s0} \varepsilon_s^{1.5}$ and $\kappa_e^{eff} = \kappa_{e0} \varepsilon_e^{1.5}$, respectively. The active surface area per electrode volume is given by $a_s = 3\varepsilon_s / r_p$. Following most literatures, here we assume that the electrolyte active coefficient $f_{\pm}$ is a constant so that $d\ln f_{\pm} / d\ln c_e = 0$. In the electrode region, the reaction current density, i, is given by the Bulter-Volmer equation shown later. In the separator region, i is zero.

The lithium ion concentration in the electrolyte is given by

$$\varepsilon_e \frac{\partial c_e}{\partial t} + \nabla \cdot (-D_e^{eff} \nabla c_e) = \frac{(1 - t_+)}{F} a_s i, \quad [3]$$

where the effective diffusivity of the electrolyte is given by $D_e^{eff} = D_{e0}\varepsilon_e^{1.5}$.

The current density between the solid phase and the electrolyte phase, i, is governed by the Bulter–Volmer equation,

$$i = i_0\left(\exp\left(\frac{\alpha F\eta}{RT}\right) - \exp\left(-\frac{(1-\alpha)F\eta}{RT}\right)\right), \quad [4]$$

and the exchange current density is given by $i_0 = Fkc_{s,surf}^{1-\alpha} c_e^{\alpha} (c_{s,\max} - c_{s,surf})^{\alpha}$. The overpotential, η, is given by

$$\eta = \Phi_s - \Phi_e - E_{eq} \quad [5]$$

Here E_{eq} is the equilibrium potential of the cathode or anode material (See Fig. A·1 in Appendix).

The lithium ion concentration in a spherical active material particle is given by

$$\frac{\partial c_s}{\partial t} = \frac{D_s}{r^2}\frac{\partial}{\partial r}\left(r^2 \frac{\partial c_s}{\partial r}\right). \quad [6]$$

The values of various parameters in the electrochemical equations are given in Table A·I Appendix.

The mechanics of the electrodes are calculated using the solid structure module in COMSOL Multiphysics 5.4. In this paper we aim to provide the electrode-level stress induced by lithium intercalation as an additional indicator to the typical electrochemical performance, rather than devoting to a study of fully coupling electrochemistry and mechanics. Therefore, like many literatures, we consider one-way coupling of the result of electrochemical process on mechanical stress generation. For simplicity, the reverse effect of stress on electrochemistry is neglected which is typically small. Lithium intercalation into an active particle causes its volume to expand. The corresponding strain, known as the eigenstrain of lithium intercalation, is related to the average lithium concentration in the particle given by[30]

$$e = \frac{\Omega}{3}(c_{s,ave} - c_{s0}). \quad [7]$$

The value of $c_{s,ave}$ is obtained by averaging the lithium concentration inside a particle obtained by Eq. 6 of the electrochemical model. The partial molar volume, Ω, of $LiMn_2O_4$ cathode material and graphite anode material are 3.497×10^{-6} m^3 mol^{-1} and 3.646×10^{-6} m^3 mol^{-1}, respectively.[31,33] Similar as thermal stress, the eigenstrain of lithium intercalation causes stress generation in the electrode.

For a porous electrode, its effective elastic modulus, E, and Poisson's ratio, ν, can be calculated based on the following fitting equations obtained from finite element simulations,[34]

$$E = E_p\left(1 - \frac{\varepsilon_e}{\beta_0}\right)^{n_0},$$
$$\nu = \xi_0 + \left(1 - \frac{\varepsilon_e}{\beta_1}\right)^{m_0}(\nu_p - \xi_0). \quad [8]$$

The bulk elastic modulus, E_p, and Poisson's ratio, ν_p, of the cathode and anode material are given in Table A·I Appendix. The fitting parameters are suggested to be $\beta_0 = 0.652$, $n_0 = 2.23$, $\beta_1 = 0.500$, $m_0 = 1.22$ and $\xi_0 = 0.140$.

The electrode-level stress, Σ_{ij}, relates to the electrode-level strain, e_{kl}, by

$$\sum_{ij} = C_{ijkl}(e_{kl} - e\delta_{kl}), \quad [9]$$

where C_{ijkl} denotes the effective elastic modulus and can be calculated by

$$C_{ijkl} = \lambda\delta_{ij}\delta_{kl} + \mu(\delta_{ik}\delta_{jl} + \delta_{il}\delta_{jk}),$$
$$\lambda = E\nu/[(1+\nu)(1-2\nu)],$$
$$\mu = E/[2(1+\nu)]. \quad [10]$$

Here δ_{ij} is the Kronecker delta.

The elastic field is solved by the equilibrium equation $\nabla \cdot \sum = 0$ in the solid structure module of COMSOL.

Simulation conditions.—In our simulations the battery was first fast charged by the constant current, constant voltage (CCCV) strategy, and then discharged until the terminal voltage decreased to the cut-off voltage. The applied charge current density was set to be 160 A m^{-2} during the CC stage. When the terminal voltage reached 4.35 V, the CC stage was terminated and the CV stage was invoked. In the CV stage, the terminal voltage was set to be a constant 4.35 V. The lower cut-off current density was set to be 80 A m^{-2}, and the charging process was stopped when the charge current density dropped below this threshold. For discharging, the applied discharge current density was set to be constant at 25 A m^{-2}, and the cut-off terminal voltage was set to be 3.5 V. The initial SOC was set to be uniformly 0.995 for the cathode (3.6 V) and uniformly 0.030 for the anode (0.6 V). Note that side reactions such as SEI formation and lithium loss are not considered in this study. We assume that an SEI is already formed and further lithium loss in one charge/discharge cycle is negligible.

The local SOC of each active particle is calculated by

$$SOC = \frac{c_{s,ave}}{c_{s,\max}}. \quad [11]$$

The boundary conditions for the solid phase potential, electrolyte potential and lithium ion concentration next to the cathode current collector ($x = L_s + L_p$) are

$$\sigma_s^{eff}\frac{\partial \Phi_s}{\partial x}\bigg|_{x=L_s+L_p} = -i_{app},$$
$$\frac{\partial \Phi_e}{\partial x}\bigg|_{x=L_s+L_p} = 0,$$
$$\frac{\partial c_e}{\partial x}\bigg|_{x=L_s+L_p} = 0, \quad [12]$$

with the sign defined as $i_{app} > 0$ for discharging.

The boundary conditions for the solid phase potential, electrolyte potential and lithium ion concentration next to the anode current collector ($x = -L_n$) are

$$\Phi_s|_{x=-L_n} = 0,$$
$$\frac{\partial \Phi_e}{\partial x}\bigg|_{x=-L_n} = 0,$$
$$\frac{\partial c_e}{\partial x}\bigg|_{x=-L_n} = 0. \quad [13]$$

The particle-level boundary conditions are

$$\frac{\partial c_s}{\partial r}\bigg|_{r=0} = 0,$$
$$D_s\frac{\partial c_s}{\partial r}\bigg|_{r=r_p} = -\frac{i}{F}. \quad [14]$$

For the mechanical calculations, fixed boundary conditions were applied to the two current collectors. The stress was set to be zero at the interface between the electrode and the separator since the separator was fairly soft. These give

$$\begin{aligned} &u_x|_{x=-L_n} = u_y|_{x=-L_n} = u_x|_{x=L_s+L_p} = u_y|_{x=L_s+L_p} = 0, \\ &u_y|_{y=W_H} = u_y|_{y=-W_H} = 0, \\ &\textstyle\sum_{xx}|_{x=0} = \sum_{xy}|_{x=0} = \sum_{xx}|_{x=L_s} = \sum_{xy}|_{x=L_s} = 0. \end{aligned} \quad [15]$$

In addition, the stress was set to be zero at the interface between the electrode and the electrolyte (i.e. surface of the channel).

Quantification of electrochemical performance and mechanical stress.—The specific energy, specific power and specific capacity during discharging are chosen to quantify the battery performance. For simplicity, we will later refer them without specifically mentioning "discharge." The specific energy (*SE*) and specific power (*SP*) are calculated by

$$\begin{aligned} SE &= \frac{\int_{t_{ds}}^{t_{de}} V_t I dt}{m}, \\ SP &= \frac{\int_{t_{ds}}^{t_{de}} V_t I dt}{m(t_{de} - t_{ds})}, \end{aligned} \quad [16]$$

where t_{ds} is the start time of discharging, t_{de} the end time, and V_t the terminal voltage during the discharging process. The discharge current is $I = i_{app}A$ where A denotes the cross-sectional area of the electrode. The cell mass is given by

$$\begin{aligned} m &= m_{Al} + m_n + m_{sep} + m_p + m_{Cu}, \\ m_p &= \rho_e V_{channel,p} + \rho_{LMO}\varepsilon_{s,p}V_{mater,p} + \rho_b\varepsilon_{b,p}V_{mater,p} \\ &\quad + \rho_e\varepsilon_{e,p}V_{mater,p}, \\ m_n &= \rho_e V_{channel,n} + \rho_{Grap}\varepsilon_{s,n}V_{mater,n} + \rho_b\varepsilon_{b,n}V_{mater,n} \\ &\quad + \rho_e\varepsilon_{e,n}V_{mater,n}, \\ m_{sep} &= \rho_e\varepsilon_{e,sep}V_{sep} + \rho_{sep}\varepsilon_{sep}V_{sep}. \end{aligned} \quad [17]$$

The subscripts "*p*", "*n*" and "*sep*" denote the cathode, anode and separator regions, respectively. The values are given in Table A·I Appendix.

The specific capacity (*SC*) of the cell is calculated by.

$$SC = \frac{I(t_{de} - t_{ds})}{m}. \quad [18]$$

The negative to positive capacity ratio (N/P ratio) is an important cell parameter. Various battery characterizes, such as lithium plating and electrode degradation, are related to this ratio.[35,36] With electrolyte channel design, the N/P ratio is given by

$$\mathrm{N/P} = \frac{c_{s,\,\max,n}\varepsilon_{s,n}V_{mater,n}}{c_{s,\,\max,p}\varepsilon_{s,p}V_{mater,p}}. \quad [19]$$

where $c_{s,\max,n}$ denotes the maximum lithium concentration in the anode particle and $c_{s,\max,p}$ denotes the maximum lithium concentration in the cathode particle.

To quantify the mechanical integrity, we employ the first principle stress which is directly related to electrode-level crack formation.

Simulation Results And Discussions

Effect of electrolyte channel length.—To investigate the effect of channel length on battery performance, two groups of simulations were performed. In the first group, the cathode channel length L_{EC} was set to be 25 μm, 50 μm, 100 μm, 150 μm and 200 μm, respectively. The anode channel length L_{EA} was set to be 200 μm. In the second group, L_{EA} was set to be 25 μm, 50 μm, 100 μm, 150 μm and 200 μm, respectively while L_{EC} was set to be 200 μm. The cathode and anode electrolyte channel width, W_{EC} and W_{EA}, were both set to be 20 μm. $W_{EA\text{-}b}$ was set to be the same as W_{EA}, and $W_{EC\text{-}b}$ was set to be same as W_{EC}. The cathode and anode active material half-width, W_C and W_A, were both set to be 10 μm. The N/P ratio of the first group of cells are 0.81, 0.86, 0.96, 1.10 and 1.29, respectively. The N/P ratio of the second group of cells are 2.04, 1.93, 1.72, 1.50 and 1.29, respectively. The curves of terminal voltage V_t during CCCV charging and of the areal capacity are shown in Fig. 2.

Figure 2a1 shows that with L_{EA} being fixed at 200 μm, the CC charging time decreases slightly with L_{EC}, causing the areal capacity of the cell to decrease slightly at the end of the CC charging process; but the CV charging time increases significantly with L_{EC}, causing the areal capacity of the cell to increase significantly with L_{EC} as the CV charging process ends. Figure 2b1 shows that the areal capacity increases monotonically from 17.81 Ah m^{-2} to 20.02 Ah m^{-2} when L_{EC} increases from 25 μm to 200 μm. The conventional-designed cell has the shortest CC and CV charging time, indicating the smallest areal capacity (14.93 Ah m^{-2} as the CCCV charging ends). Figure 2a2 shows that with L_{EC} being fixed at 200 μm, the CC charging time increases with L_{EA} while the CV charging time decreases with L_{EA}. Figure 2b2 shows that the areal capacity at the end of CCCV charging first decreases and then increases with L_{EA}. The largest areal capacity is 20.02 Ah m^{-2} as L_{EA} reaches 200 μm. Besides, the CC charging time of the conventional-designed cell is close to that of the cell with the shortest channel of $L_{EA} = 25$ μm, but its CV charging time is significantly shorter than the cell with the channel.

The local state of charge of the cathode and anode material is analyzed at the end of CCCV charging. For the conventional-designed cell, the local SOC of the anode material decreases monotonically from the separator toward the anode current collector along the electrode thickness direction, as shown in Fig. 3a. The material adjacent to the separator has the highest SOC and the high SOC region (SOC $\geqslant$ 0.8) is fairly narrow. For the cathode, the material adjacent to the separator has the lowest SOC, while a large amount of material far from the separator has high SOC. These results indicate that for the thick electrode, only a small amount of cathode material adjacent to the separator gets deintercalated during fast charging. Similarly, only a small amount of anode material adjacent to the separator gets well intercalated (SOC $\geqslant$ 0.8). A large amount of the anode material far from the separator is poorly charged (SOC $<$ 0.4). Thus the conventional-designed cell has poor performance as shown later. In the following we refer SOC $\geqslant$ 0.8 as the high charging state and SOC $<$ 0.4 as the low charging state when talking about anode.

Figure 3a1 shows that with L_{EA} being fixed at 200 μm, the amount of anode material with high charging state first increases (blue line moves left) and then decreases slightly (blue line moves right) with L_{EC}. The amount of anode material with low charging state decreases monotonically, indicating that the anode charging state becomes more uniform. For the cathode, the SOC at each position decreases with L_{EC}, suggesting that longer channels make it easier for the cathode particles to de-intercalate lithium ions. Figure 3a2 shows that with L_{EC} being fixed at 200 μm, the amount of anode material with high charging state first increases and then decreases slightly with L_{EA}, while the amount of anode material with low charging state decreases significantly with L_{EA}. These trends indicate that the anode charging state becomes more uniform. For the cathode, the SOC at each position first decreases slightly then increases slightly with L_{EA}, suggesting that the lithium ion deintercalation at the cathode is not affected much by the anode electrolyte channel.

The lithium ion concentration distribution in the electrolyte at the end of CCCV charging is also shown in Fig. 3b. With L_{EA} being

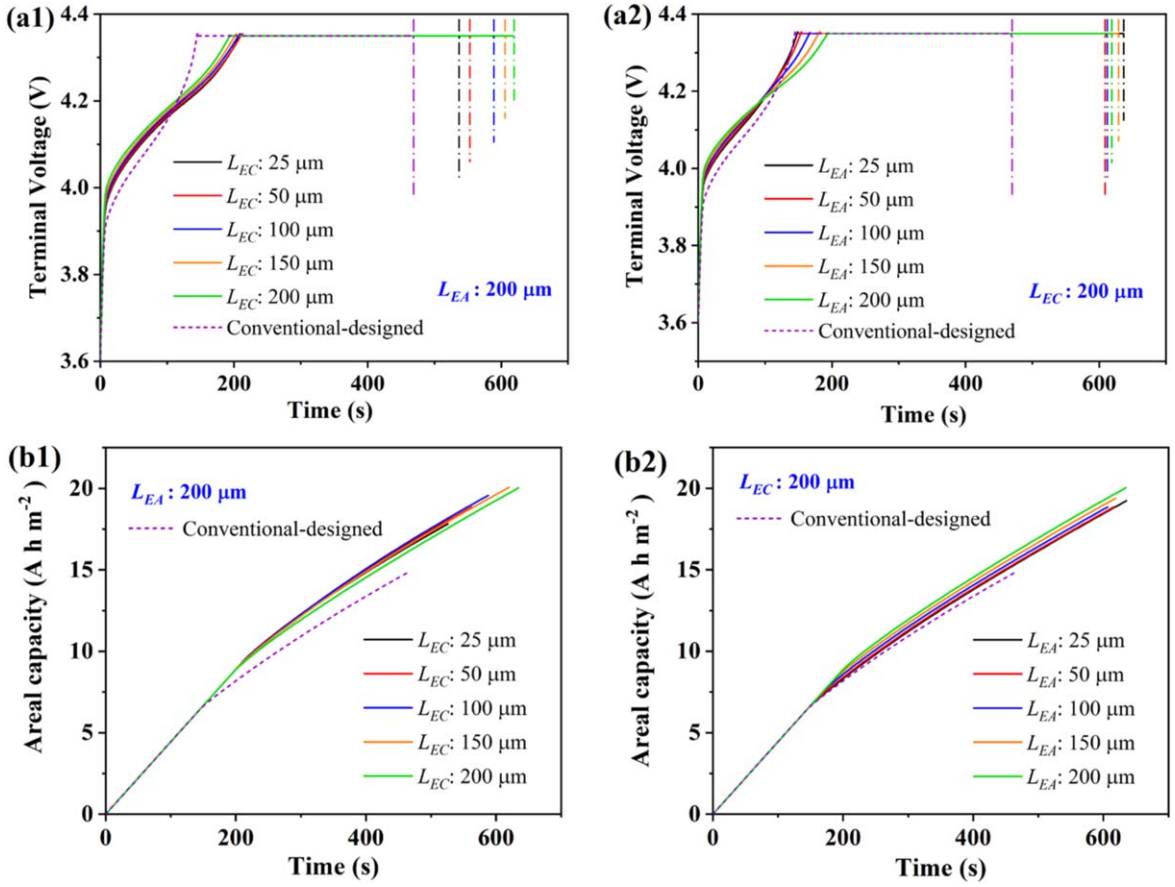

Figure 2. The profiles of (a) terminal voltage and (b) areal capacity for cells with different electrolyte channel length during CCCV charging. Left: L_{EA} fixed at 200 μm with varying L_{EC}. Right: L_{EC} fixed at 200 μm with varying L_{EA}. The vertical dash-dot lines in (a) denote the cut-off time when the entire CCCV charging ends. The color of each dash-dot line matches the color of the corresponding solid line terminal voltage curve in the figure.

fixed, the lithium ion concentration in the electrolyte at each position in the cathode region decreases significantly with L_{EC} (bottom figure in Fig. 3b1) while the concentration at each position in the anode region increases slightly. The concentration gradient in the electrolyte along the electrode thickness direction decreases with L_{EC}, suggesting that longer channels make lithium ions distribute more uniformly in the electrolyte. With L_{EC} being fixed, the lithium ion concentration in the electrolyte at each position of the anode region increases with L_{EA} (bottom figure in Fig. 3b2), and so does the concentration in the electrolyte at each position of the cathode region.

Figure 4 shows the discharge *SE*, *SP* and *SC* obtained by calculating the discharge process after the completion of CCCV charging. It can be seen from Fig. 4a that with L_{EA} being fixed, *SE*, *SP* and *SC* all increase monotonically with L_{EC}. With the shortest channel, the *SE*, *SP* and *SC* values are 19.48%, 9.93% and 18.98% lower than those with the longest channel. However, even with the shortest channel, the *SE*, *SP* and *SC* values are 32.90%, 5.40% and 31.95% higher than those of the conventional-designed cell. With L_{EC} being fixed, the *SE* and *SC* values first decrease slightly and then increase with L_{EA}, as shown in Fig. 4b. The *SP* value increases monotonically with L_{EA}. Even with the shortest channel, the *SE*, *SP* and *SC* values are 50.21%, 13.34% and 49.01% higher than those of the conventional-designed cell. With the shortest channel, the *SE*, *SP* and *SC* values are 6.60%, 3.52% and 6.21% lower than those with the longest channel. These observations indicate that by changing the electrolyte channel length alone, the battery specific energy, specific power, and specific capacity can significantly exceed the conventional-designed battery cell. The cell performance appears to be more sensitive to the cathode electrolyte channel length than to the anode electrolyte channel length.

The first principal stress inside the battery electrodes during charging was analyzed to investigate the effect of electrolyte channel length on mechanical integrity. The first principal stress is directly related to electrode-level crack formation in-between active material particles. Figure 5a shows the contours of first principal stress distribution in the conventional-designed cell at the end of the CCCV charging. We can observe that the first principal stress in the cathode is significantly larger than that in the anode. In addition, the first principal stress is positive in the cathode while negative in the anode. This suggests that during charging, the cathode undergoes tensile loading, which is consistent with Li-ion deintercalation at cathode and that the associated shrinkage of particle volume is constrained by the current collector. The anode material undergoes compression by the constraint of current collector against particle expansion due to Li-ion interaction. Simulations have shown that the maximum first principal stress occurs in the cathode at the location of the cathode/separator interface for both conventional-designed cells and cells with electrolyte channels, as a result of more Li-ion deintercalation at this location. Therefore, we compare the first principal stress at the cathode/separator interface for various channel design to evaluate the mechanical integrity.

Figure 5b shows the first principal stress in the cathode at the location of the cathode/separator interface as a function of SOC for the conventional-designed cell and cells with different anode channel length, L_{EA}. Here the average SOC is calculated on the entire cathode volume to reflect the overall state. We can observe that the maximum first principal stress in the cathode is significantly lower with electrolyte channels than that in the conventional-designed cell. In addition, the first principal stress increases rapidly with SOC in the conventional-designed cell, while the trend is less steep in the cell with channels. When the average cathode SOC

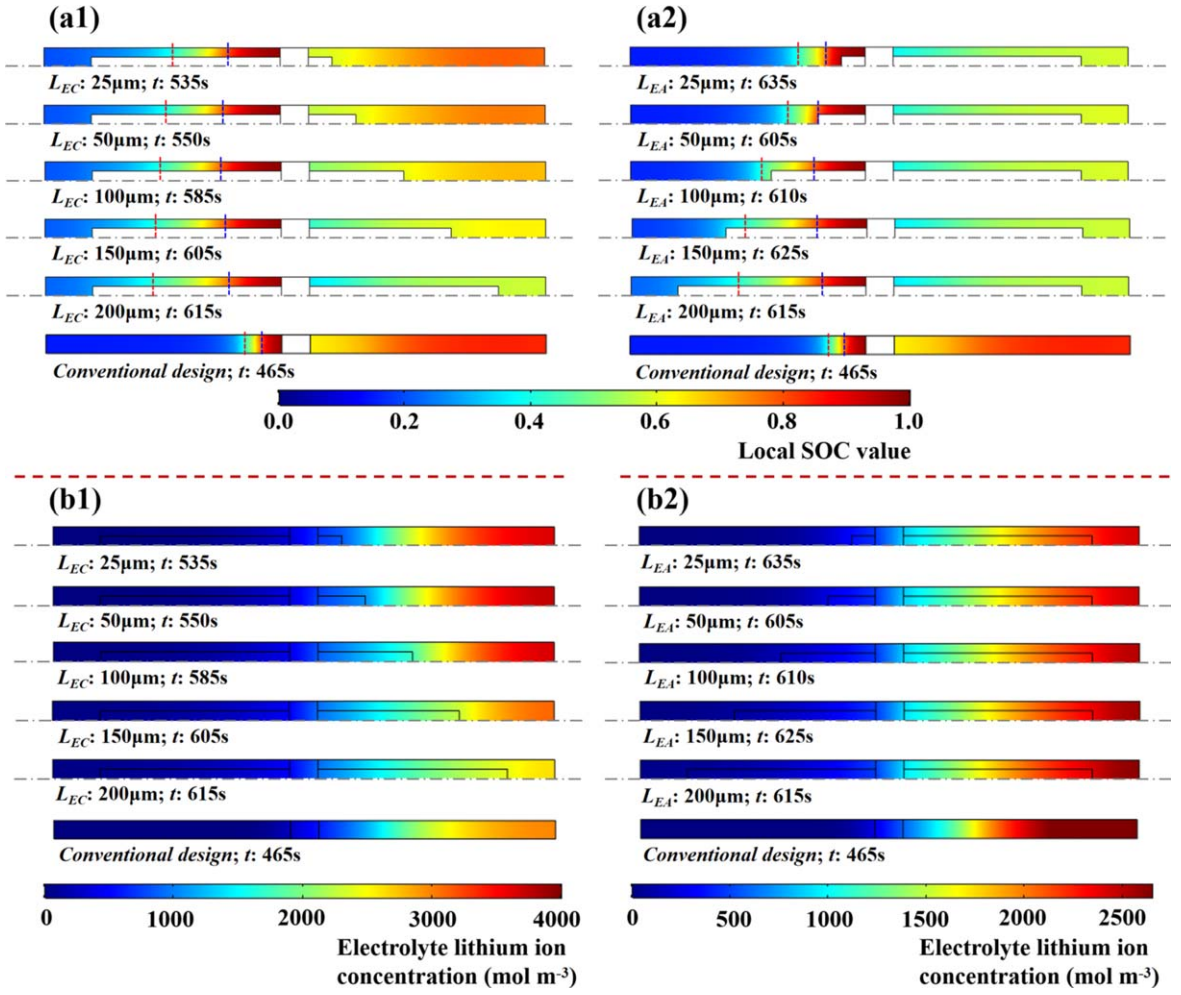

Figure 3. The distribution of (a) local SOC in the electrode and (b) lithium ion concentration in the electrolyte at the end of CCCV charging. The time *t* shows the end time of CCCV charging, which is different for different cases. Left: L_{EA} fixed at 200 μm with varying L_{EC}. Right: L_{EC} fixed at 200 μm with varying L_{EA}. In the top figures the red dash line denotes the boundary of SOC = 0.4 while the blue dash line denotes the boundary of SOC = 0.8.

reduces to 0.78 (which is the level that a conventional-designed cell would research the end of charging), the first principal stress of the conventional-designed cell is 3.06 MPa larger than that of the cell with electrolyte channels of L_{EA} = 25 μm and L_{EC} = 200 μm, indicating that electrolyte channels can significantly reduce the cathode stress near the separator. Thus, the introduction of electrolyte channels has a positive effect on the mechanical integrity of the cell.

Effect of electrolyte channel width.—Three groups of simulations were performed to investigate the effect of the electrolyte channel width. In the first group, W_{EA} and W_{EC} were set to be the same and their values were 5μm, 10 μm, 20 μm, 40 μm and 80 μm. In the second group, the cathode had no electrolyte channel while W_{EA} was set to be 5 μm, 10 μm, 20 μm, 40 μm and 80 μm. In the third group, the anode had no electrolyte channel while W_{EC} was set to be 5 μm, 10 μm, 20 μm, 40 μm and 80 μm. L_{EA} and/or L_{EC} were set to be 200 μm. $W_{EA\text{-}b}$ was set equal to W_{EA}, $W_{EC\text{-}b}$ was set equal to W_{EC}. W_C and/or W_A were set to be 20 μm. The N/P ratio of the first group of cells are all 1.29. The N/P ratio of the second group of cells are 1.53, 1.75, 2.14, 2.76 and 3.57, respectively. The N/P ratio of the third group of cells are 1.08, 0.94, 0.77, 0.60 and 0.46, respectively.

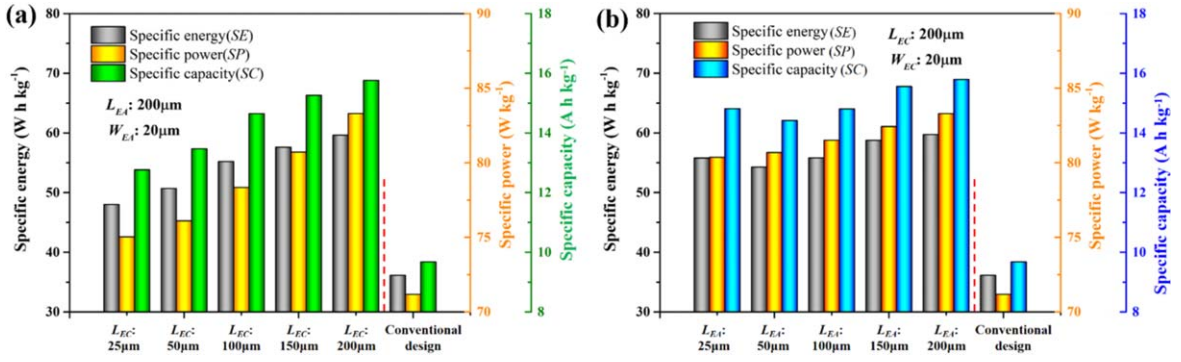

Figure 4. Cell performance as a function of electrolyte channel length. (a) L_{EA} fixed at 200 μm with varying L_{EC} (b) L_{EC} fixed at 200 μm with varying L_{EA}.

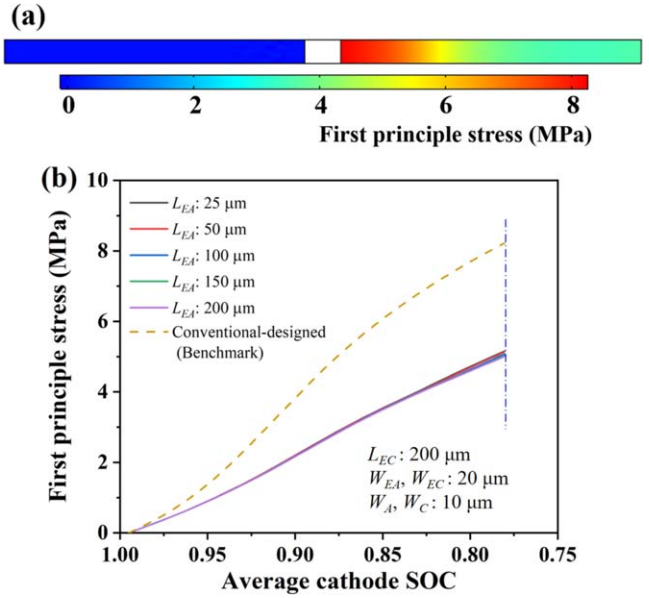

Figure 5. (a) Contour of the first principal stress in the conventional-designed cell. The maximum first principal stress occurs in the cathode at the location of the cathode/separator interface. (b) First principal stress in the cathode at the location of the cathode/separator interface as a function of SOC for the conventional-designed cell and cells with different anode channel length, L_{EA}. (L_{EC}: 200 μm; W_{EA}, W_{EC}: 20 μm; W_A, W_C: 10 μm).

The simulation results of terminal voltage curves during the CCCV charging process are presented in Fig. 6a.

For the cell with concurrent cathode and anode channels, the CC and CV charging time first increases and then decreases with W_{EA} and W_{EC} (Fig. 6a1). The maximum CCCV charging time occurs when W_{EA} and W_{EC} are 10 μm. The CCCV charging time is even shorter than that of the conventional-designed cell when W_{EA} and W_{EC} reach 80 μm. Similarly, as shown in Fig. 6b1, the areal capacity at the end of CCCV charging first increases to a maximum of 20.95 Ah m^{-2} as W_{EA} and W_{EC} reach 10 μm. Then, the areal capacity decreases to a minimum of 8.85 Ah m^{-2} as W_{EA} and W_{EC} reach 80 μm. This minimum is 40.72% lower than the areal capacity of the conventional-designed cell (14.93 Ah m^{-2}). When only one of the electrode has channels, the maximum CCCV charging time occurs when W_{EA} = 10 μm or W_{EC} = 20 μm (Figs. 6a2 and 6a3). When W_{EA} reaches 40 μm or W_{EC} reaches 80 μm, the CCCV charging time is shorter than that of the conventional-designed cell. Figures 6b2 and 6c2 show that the areal capacity for a cell with a flat cathode reaches its maximum of 17.65 Ah m^{-2} as W_{EA} reaches 10 μm, while the areal capacity for a cell with a flat anode reaches its maximum of 19.49 Ah m^{-2} as W_{EC} reaches 20 μm. These indicate that the maximum areal capacity of a cell is larger with electrolyte channels in both the anode and cathode, than that with channels in only one of them.

Now consider the local SOC after CCCV charging. For the cell with both cathode and anode channels, the amount of anode material with high charging state first increases and then decreases rapidly with W_{EA} and W_{EC} (Fig. 6c1). The amount of anode material with low charging state first decreases and then increases, suggesting that the charging state of the anode material becomes more uniform with appropriate channel width. For the cathode, the SOC at each position first decreases and then increases rapidly with W_{EA} and W_{EC}, indicating that it is more difficult for Li-ion de-intercalation when W_{EA} and W_{EC} exceed 20 μm.

For the cell with only anode channels, the amount of anode material with high charging state increases rapidly with W_{EA} (Fig. 6c2), and the amount of anode material with low charging state decreases monotonically and rapidly with W_{EA}. In the cathode, the SOC at each position increases slightly with W_{EA}, indicating that it is slightly getting more difficult for the Li-ion to deintercalate. For the cell with only cathode channel, the amount of anode material charging state is slightly affected by W_{EC}. The anode material with high charging state decreases with W_{EC} (Fig. 6c3), and the amount of anode material with low charging state first decreases slightly and then increases slightly. By contrast, the cathode SOC at each position decreases dramatically with W_{EC}. These results show that the local SOC has more complicated dependence on the channel width.

The dependence of *SE*, *SP* and *SC* on channel width is presented in Fig. 7. For the cell having both anode and cathode electrolyte channels of the same size, *SE* and *SC* first increase with W_{EA} and W_{EC} when they increase from 5 μm to 10 μm, and then decrease rapidly when they change from 20 μm to 80 μm (Fig. 7a). The maximum *SE* and *SC* are 65.99% and 64.32% larger than those of the conventional-designed cell. However, the *SE* and *SC* are 27.36% and 27.61% lower than those of the conventional-designed cell when W_{EA} and W_{EC} are 80 μm. The *SP* increases monotonically with W_{EA} and W_{EC}, and is 27.74% larger than that of the conventional-designed cell when they are 80 μm.

For the cell with only anode electrolyte channel, the changing pattern of *SE*, *SC* and *SP* with W_{EA} is similar to that with concurrent cathode and anode electrolyte channels. The maximum *SE*, *SP* and *SC* of the cell with anode channel are 25.42%, 24.72%, and 5.78% larger than those of the conventional-designed cell, respectively (Fig. 7b). For the cell with only cathode electrolyte channel, *SE* and *SC* first increase with W_{EC} till about 10 μm or 20 μm, and then decrease rapidly (Fig. 7c). The *SE* and *SC* are still larger than those of the conventional-designed cell when W_{EC} reaches 80 μm. The *SP* increases monotonically with W_{EC}. The maximum *SE*, *SC* and *SP* of the cell with cathode channel are 55.80%, 54.39%, and 20.36% larger than those of the conventional-designed cell, respectively.

These results suggest that with changing electrolyte channel width, the cell performance can be significantly higher or lower than the conventional-designed cell. There exists optimal channel widths for maximum specific energy and specific capacity, while the specific power tends to change monotonically with the channel width.

The first principal stress in the cathode at the location of the cathode/separator interface as a function of SOC were investigated for various electrolyte channel width. Figure 8 shows that with increasing electrolyte channel width, the first principal stress decreases rapidly. The magnitude is much smaller than that in the conventional-designed cell. When the cathode average SOC reduces to 0.78, the first principal stress in the conventional-designed cell is 2.15 MPa larger than that of the cell with W_{EA} =W_{EC} = 5 μm, and 3.82 MPa larger than that of the cell with W_{EA} = W_{EC} = 80 μm. These suggest that increasing the electrolyte channel width can significantly reduce the cathode stress.

Effect of active electrode material width.—To investigate the effect of active electrode material width on the cell performance, three groups of simulations were performed. In the first group, the active anode and cathode material half-width W_A and W_C were set to be the same, with values of 10 μm, 20 μm, 40 μm, 80 μm and 160 μm. In the second group, the cathode had no channel, while the active anode material half-width W_A was set to be 10 μm, 20 μm, 40 μm, 80 μm and 160 μm. In the third group, the anode had no channel, while the active cathode material half-width W_C was set to be 10 μm, 20 μm, 40 μm, 80 μm and 160 μm. L_{EA} and/or L_{EC} were set to be 200 μm. W_{EA} and/or W_{EC} were set to be 20 μm. W_{EA} and $W_{EA\text{-}b}$ were set to be same. W_{EC} and $W_{EC\text{-}b}$ were set to be the same. The N/P ratio of the first group of cells are all 1.29. The N/P ratio of the second group of cells are 2.76, 2.14, 1.75, 1.53 and 1.41, respectively. The N/P ratio of the third group of cells are 0.60, 0.77, 0.94, 1.08 and 1.17, respectively. The terminal voltage curves during the CCCV charging process are presented in Fig. 9a.

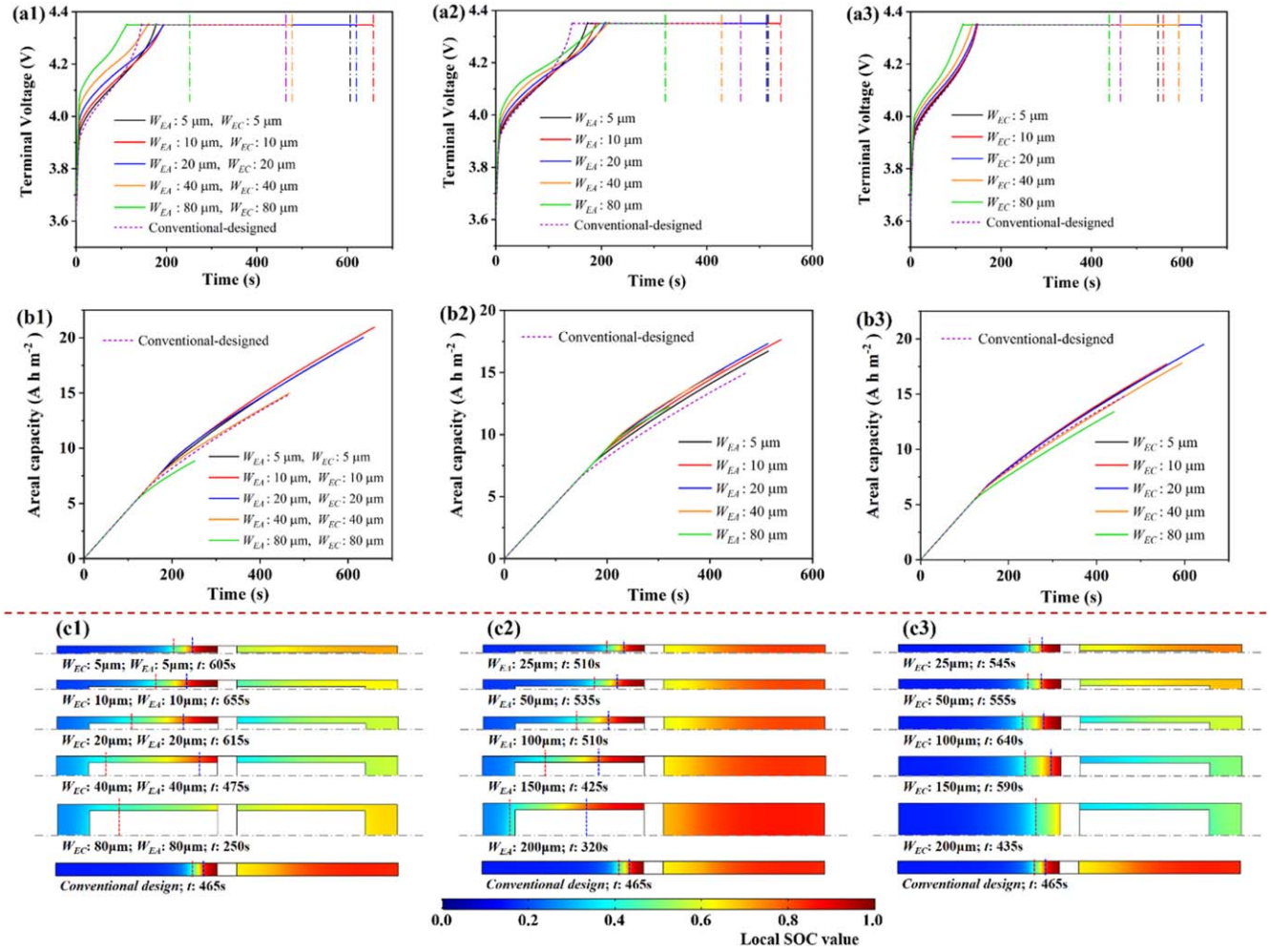

Figure 6. (a) The terminal voltage and (b) areal capacity profiles of the cell during CCCV fast charging with various electrolyte channel width. Left: both cathode and anode channels, $L_{EA} = L_{EC} = 200$ μm. Middle: anode channel only, $L_{EA} = 200$ μm. Right: cathode channel only, $L_{EC} = 200$ μm. The vertical dash-dot lines in (a) denote the cut-off time when the entire CCCV charging ends. The color of each dash-dot line matches the color of the corresponding solid line terminal voltage curve in the figure. (c) The local SOC in the electrode at the end of CCCV charging. The time t shows the end time of CCCV charging, which is different for different cases. (The red dash line denotes the boundary of 0.4 SOC, the blue dash line denotes the boundary of 0.8 SOC). Left: both cathode and anode channels, $L_{EA} = L_{EC} = 200$ μm. Middle: anode channel only, $L_{EA} = 200$ μm. Right: cathode channel only, $L_{EC} = 200$ μm.

The CC and CV charging time both first increase then decrease with the active electrode material half-width W_A and W_C for concurrent channels in the anode and cathode (Fig. 9a1). Similarly, Fig. 9b1 shows that the areal capacity first increases and then decreases with W_A and W_C. The maximum areal capacity reaches 20.42 Ah m^{-2} when W_A and W_C are both 20 μm. When there is only channel in the anode, the CC charging time decreases monotonically with W_A, while the CV charging time first increases rapidly and then decreases with W_A (Fig. 9a2). The CCCV charging time reaches its maximum when W_A is 20 μm. The areal capacity also reaches its maximum of 17.36 Ah m^{-2} when W_A is 20 μm, as shown in Fig. 9b2. When there is only channel in the cathode, the CC charging time increases slightly with W_C, while the CV charging time first increases and then decreases with W_C (Fig. 9a3). The CCCV charging time reaches its maximum when the W_C is 10 μm. The areal capacity also reaches its maximum of 19.50 Ah m^{-2} when W_C is 10 μm, as shown in Fig. 9b3. With the electrolyte channel width fixed and keeping increasing the active electrode material width, the areal capacity will approach to that of the conventional-designed cell.

For the local the local SOC after CCCV charging, the amount of anode material with high charging state first increases and then decreases with W_A and W_C for concurrent channels in the anode and cathode (Fig. 9c1). The amount of anode material with low charging state increases monotonically. In the cathode, the SOC at each position increases monotonically with W_A and W_C, indicating that it is getting increasingly difficult for the cathode to release Li-ions.

When there is only anode channel, the amount of anode material with high charging state decreases rapidly with W_A (Fig. 9c2). The amount of anode material with low charging state increases dramatically. The SOC at each position of the cathode only increases slightly, indicating that the anode active electrode material width does not affect much the deintercalation at the cathode. When there is only cathode channel, the amount of anode material with high charging state first increases slightly and then decreases slightly with W_C (Fig. 9c3), indicating that the cathode active electrode material width does not affect the anode charging state much. The SOC at each position of the cathode increases rapidly with W_C. The results suggest that changing the active electrode material width can bring a complex effect on the local charging state. It should be noted that when the active electrode material width is large enough (e.g., larger than 80 μm), the SOC distribution along the x-axis is similar to that the conventional-designed cell.

Figure 10 shows the *SE*, *SC* and *SP* for various active electrode material width. For the cell having concurrent anode and cathode electrolyte channels of the same size, *SE* and *SC* first increase with W_A and W_C when they change from 5 μm to 10 μm, and then

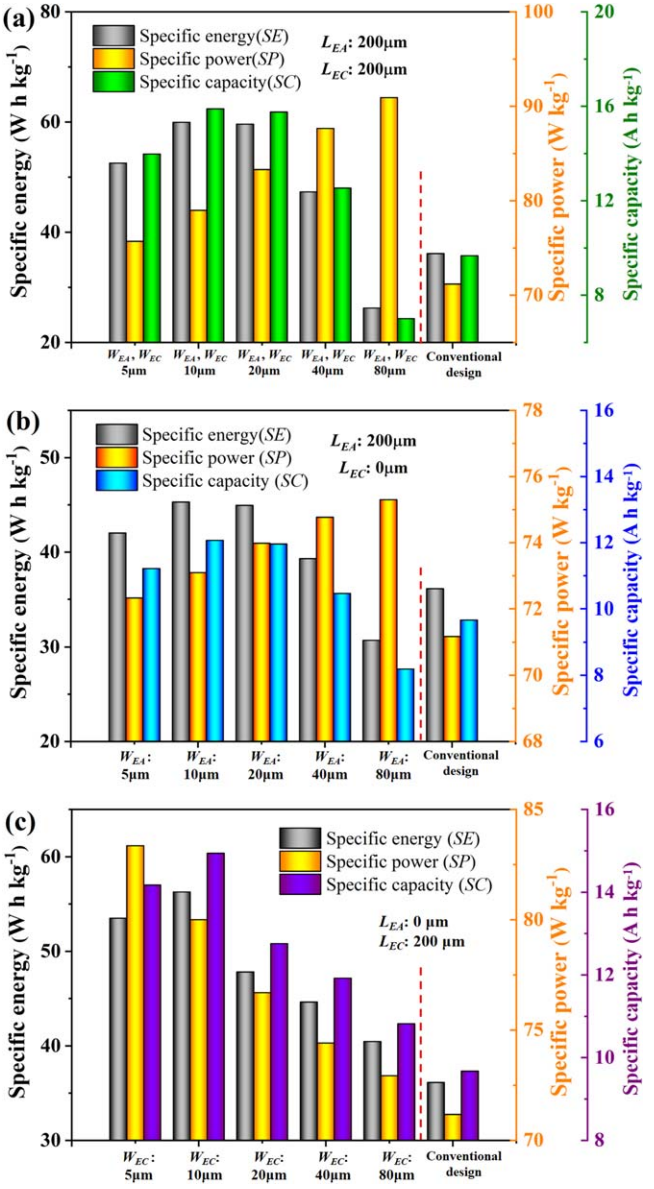

Figure 7. The performance at different electrolyte channel width for a cell having (a) concurrent cathode and anode electrolyte channels, (b) only anode electrolyte channel (c) only cathode electrolyte channel.

decrease when they change from 10 μm to 80 μm (Fig. 10a). The *SP* decreases monotonically with W_A and W_C. The maximum *SE*, *SC* and *SP* are 65.05%, 62.87% and 23.17% larger than those of the conventional-designed cell, respectively. For the cell with only anode or electrode electrolyte channel, the changing patterns of *SE*, *SC* and *SP* with W_A or W_C are similar as those of concurrent channels (Figs. 10b and 10c). The maximum *SE*, *SC* and *SP* of the cell with only anode channel are 24.45%, 23.57% and 5.03% larger than those of the conventional-designed cell, respectively. The maximum *SE*, *SC* and *SP* of the cell with only cathode channel are 55.83%, 54.49% and 17.11% larger than those of the conventional-designed cell, respectively.

These results indicate that by changing the active electrode material width, improved specific energy and specific capacity can be obtained. It should be noted that when the active electrode material width is large enough, the cell performance becomes close to that of the conventional-designed cell since the electrolyte channels are too sparse to affect the cell performance.

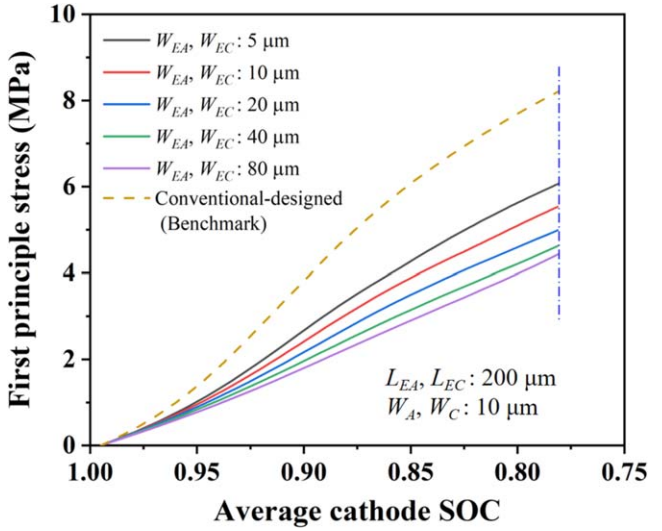

Figure 8. First principal stress in the cathode at the location of the cathode/separator interface as a function of SOC for the conventional-designed cell and cells with different anode and cathode channel width, W_{EA}, W_{EC} (L_{EA}, L_{EC}: 200 μm; W_A, W_C: 10 μm).

The first principal stress in the cathode at the location of the cathode/separator interface as a function of SOC were investigated for various active electrode material width. Figure 11 shows that with increasing active electrode material width, the principal stress increases to approach that in the conventional-designed cell. When the cathode SOC reduces to 0.78, the first principal stress in the conventional-designed cell is 3.62 MPa larger than that of the cell with $W_A = W_C = 5$ μm.

Effect of simultaneously changing electrolyte channel width and active electrode material width.—The previous two sections show that changing the electrolyte channel width and the active electrode material width has a significant effect on the cell performance. Here we consider the effect of changing them simultaneously to investigate the design option. The ratio of the electrolyte channel width to the cell periodic width (W_{EA}/W_H and W_{EC}/W_H) was introduced. Two groups of simulations were performed. W_{EA} was set to be constant at 20 μm in the first group, while W_{EC} was set to be 5 μm, 10 μm, 20 μm, 40 μm and 80 μm respectively. The ratio W_{EC}/W_H was 0.13, 0.25, 0.50, 0.67 and 0.80, respectively. The ratio W_{EA}/W_H was 0.50, 0.50, 0.50, 0.33 and 0.20 respectively. In the second group, W_{EC} was set to be constant at 20 μm, while W_{EA} was set to be 5 μm, 10 μm, 20 μm, 40 μm and 80 μm, respectively. The ratio W_{EA}/W_H was 0.13, 0.25, 0.50, 0.67 and 0.80, respectively. The ratio W_{EC}/W_H was 0.50, 0.50, 0.50, 0.33 and 0.20 respectively. L_{EC} and L_{EA} remained constant at 200 μm in both groups. $W_{EA}/W_{EA\text{-}b}$ and $W_{EC}/W_{EC\text{-}b}$ were set to be 1. The *SE*, *SP* and *SC* of the cells were calculated and are presented in Fig. 12.

By simultaneously increasing W_{EA}/W_H and decreasing W_{EC}/W_H, *SE*, *SP* and *SC* first increase slightly and then decrease rapidly (Fig. 12a). The largest *SE*, *SP* and *SC* are 80.14%, 17.03% and 77.56% larger than those of the conventional-designed cell, respectively. The minimum *SE* and *SC* are 4.68% and 5.17% lower than that of the conventional-designed cell, respectively, suggesting that design optimization can play a large role here. By increasing W_{EC}/W_H and decreasing W_{EA}/W_H simultaneously, *SE* and *SC* first increase then decrease (Fig. 12b), while *SP* increases monotonically. The largest *SE*, *SP* and *SC* are 65.09%, 22.52% and 62.87% larger than those of the conventional-designed cell, respectively. These phenomena indicate that by simultaneously changing the electrolyte channel width and the active electrode material width, the battery performance can be significantly changed. Besides, the optimized specific energy, specific power, and specific capacity are much higher compared to the case

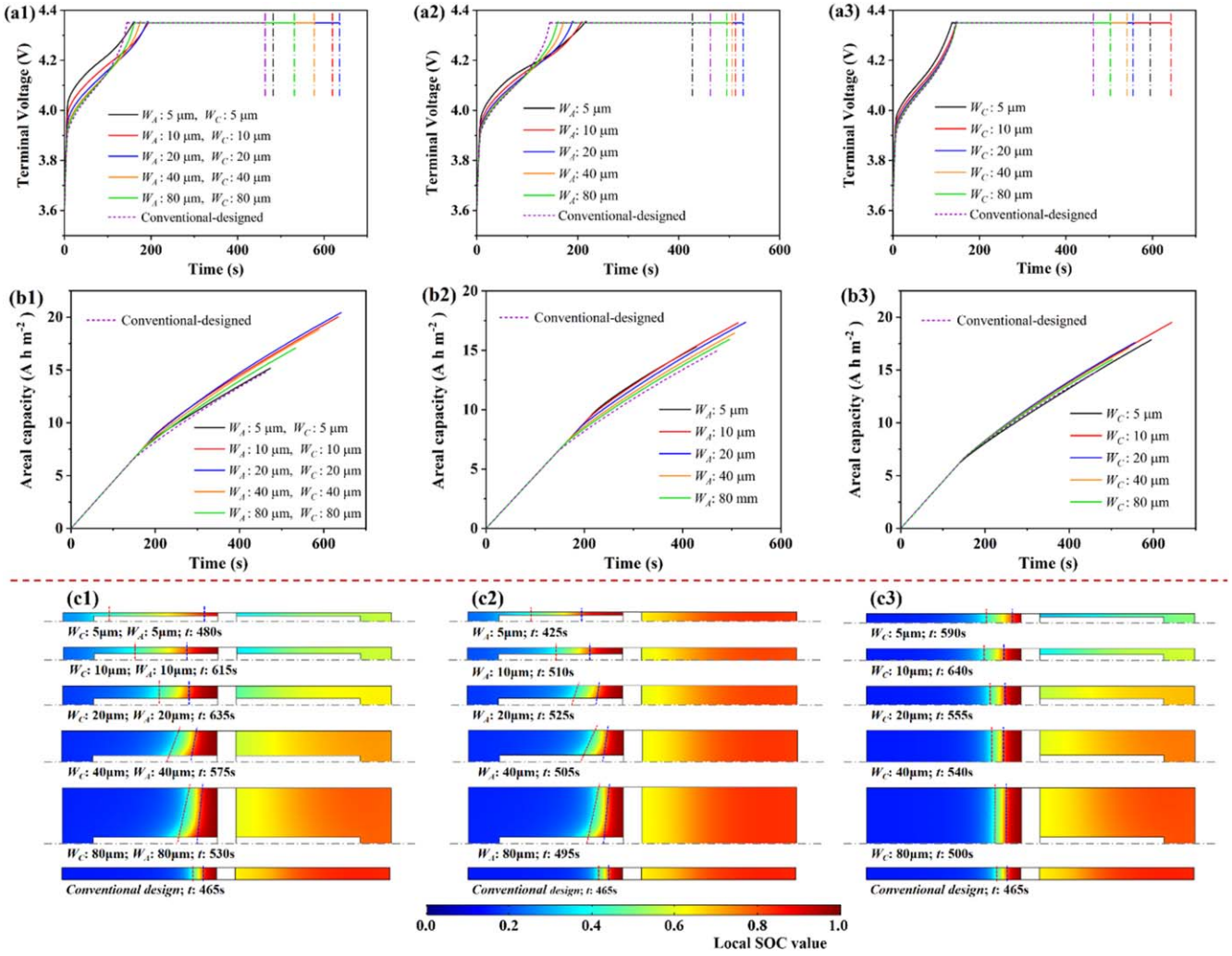

Figure 9. (a) The terminal voltage and (b) areal capacity profiles of the cell during CCCV fast charging with various active electrode material width. Left: both cathode and anode channels, $L_{EA} = L_{EC} = 200$ μm. Middle: anode channel only, $L_{EA} = 200$ μm. Right: cathode channel only, $L_{EC} = 200$ μm. The vertical dash-dot lines in (a) denote the cut-off time when the entire CCCV charging ends. The color of each dash-dot line matches the color of the corresponding solid line terminal voltage curve in the figure. (c) The local SOC in the electrode at the end of CCCV charging. The time t shows the end time of CCCV charging, which is different for different cases. (The red dash line denotes the boundary of 0.4 SOC, the blue dash line denotes the boundary of 0.8 SOC). Left: both cathode and anode channels, $L_{EA} = L_{EC} = 200$ μm. Middle: anode channel only, $L_{EA} = 200$ μm. Right: cathode channel only, $L_{EC} = 200$ μm.

when only one of the two is changed (e.g. sections "Effect of electrolyte channel width" and "Effect of active electrode material width"). Thus simultaneously tuning electrolyte channel width and active electrode material width provides better opportunity in improving the battery performance.

Another way to change the electrolyte channel width and the active electrode material width simultaneously is by the taper design of the electrolyte channel to make $W_{EA\text{-}b}$ and $W_{EC\text{-}b}$ smaller than W_{EA} and W_{EC}, respectively. The tapering degrees of the cathode and anode electrolyte channels are quantified by $W_{EC}/W_{EC\text{-}b}$ and $W_{EA}/W_{EA\text{-}b}$, respectively. A group of simulations was introduced to explore the effect of electrolyte channel tapering degree on battery performance. W_{EA} and W_{EC} were chosen to be 40 μm, while $W_{EA\text{-}b}$ and $W_{EC\text{-}b}$ were chosen to be the same with values of 40 μm, 20 μm, 10 μm, 8 μm and 4 μm. The corresponding $W_{EA}/W_{EA\text{-}b}$ and $W_{EC}/W_{EC\text{-}b}$ were the same, with values of 1.0, 2.0, 4.0, 5.0 and 10.0, respectively. $W_{EA}/W_{EA\text{-}b} = 1$ or $W_{EC}/W_{EC\text{-}b} = 1$ corresponds to an electrolyte channel without taper. L_{EA} and L_{EC} were chosen to be 200 μm. W_A and W_C were chosen to be 10 μm, making the cell periodic width W_H to be fixed at 60 μm. The *SE*, *SP* and *SC* of the cell with electrolyte channels of various tapering degrees are presented in Fig. 13.

Figure 13 shows that *SE* and *SC* first increase and then decrease slightly as $W_{EA}/W_{EA\text{-}b}$ and $W_{EC}/W_{EC\text{-}b}$ increase simultaneously from 1.0 to 4.0 and from 4.0 to 10.0, respectively. The maximum *SE* and *SC* are 16.38% and 16.53% larger than those of the cell without electrolyte channel tapering design, respectively, and 49.34% and 47.98% larger than those of the conventional-designed cell, respectively. *SP* decreases monotonically with $W_{EA}/W_{EA\text{-}b}$ and $W_{EC}/W_{EC\text{-}b}$. These phenomena indicate that by introducing the electrolyte channel tapering design, the battery specific energy and specific capacity are improved, while the specific power is reduced.

Next we consider how the tapering design affects the maximum first principal stress. $W_{EA}/W_{EA\text{-}b}$ and $W_{EC}/W_{EC\text{-}b}$ were set to be the same, taking values of 1.0, 2.0, 4.0, 8.0 and 10.0, respectively. Figure 14 shows that the first principal stress in the conventional-designed cell increases more rapidly with SOC than that of the cell with electrolyte channels. The first principal stress increases with the tapering degree, but at a reduced pace. When the average cathode SOC reduces to 0.78, the first principal stress in the conventional-designed cell is 2.51 MPa larger than that of the cell with channels of $W_{EA}/W_{EA\text{-}b} = W_{EC}/W_{EC\text{-}b} = 10.0$.

Deep Artificial Neural Network Aided Design

Setup of design system.— *Deep artificial neural network (DNN).*—Results in the previous sections show that the electrolyte

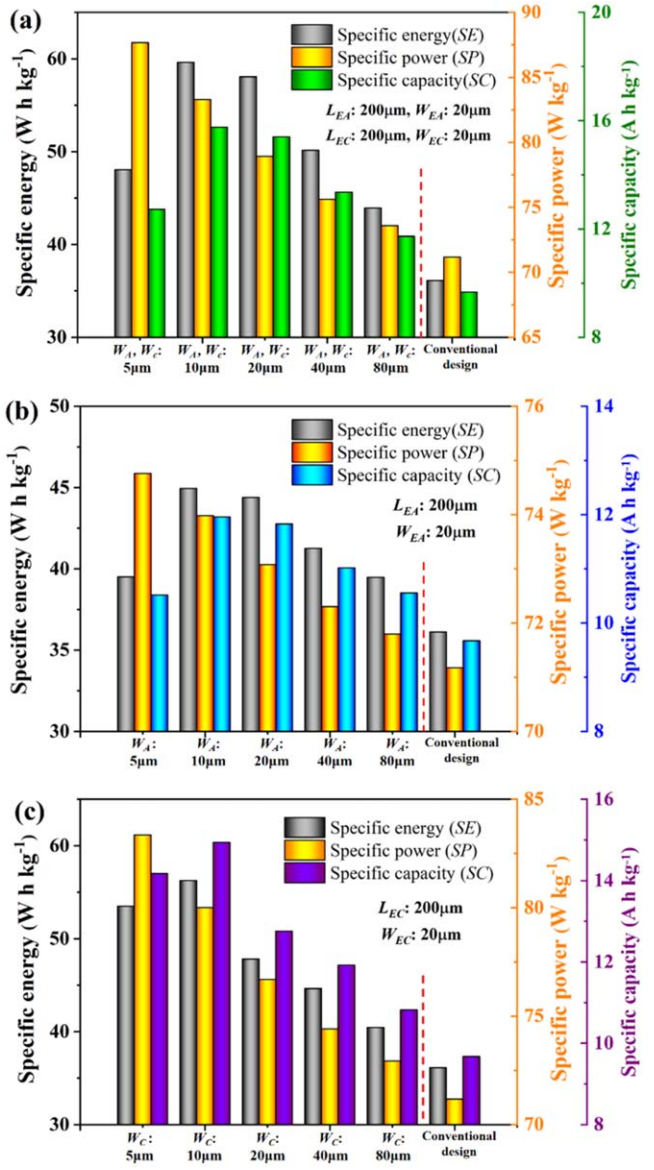

Figure 10. The performance at different active electrode material width for a cell having (a) concurrent cathode and anode electrolyte channels, (b) only anode electrolyte channel (c) only cathode electrolyte channel.

channel length, width, tapering degree and the active electrode material width all have significant effects on the battery cell performance. We have only considered their individual effects and demonstrated preliminary yet rich effect of combined electrolyte channel width and active electrode material width. In Li-ion battery design, the geometrical parameters of the electrolyte channel offer a huge design space of various combination of the parameter values. Therefore, it is necessary to develop an approach to efficiently evaluate the cell performance for arbitrary electrode geometrical parameter combinations to search for the optimized design. Using finite element simulations to evaluate the cell performance for all these scenarios are impractical due to the large amount of computations. Here we first develop a machine learning system based on DNN to predict the cell performance for arbitrary combination of electrolyte channel parameters. Then we use the system for design optimization.

Figure 15a shows a schematic of the deep artificial neural network to predict cell performance with 7 electrolyte channel

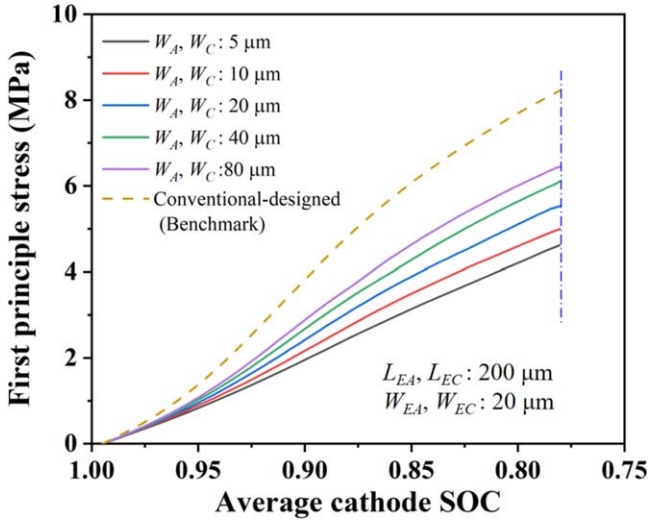

Figure 11. First principal stress in the cathode at the location of the cathode/separator interface as a function of SOC for the conventional-designed cell and cells with various active electrode material width, W_A, W_C (L_{EA}, L_{EC}: 200 μm; W_{EA}, W_{EC}: 20 μm).

design parameters as input, including L_{EC}, L_{EA}, W_H, W_{EA}/W_H, W_{EC}/W_H, $W_{EA}/W_{EA\text{-}b}$ and $W_{EC}/W_{EC\text{-}b}$. These parameters can completely determine the geometry of a tapered electrolyte channel. Figure 15b shows the implementation using the machine learning toolbox in MATLAB, which includes 40, 20, and 10 neurons in the first, second, and third hidden layer, respectively. This network has three outputs: specific discharge energy, specific discharge power and specific discharge capacity of the cell. For the DNN training process, we generated 20000 groups of dataset based on FEM of the equations in the section "Modelling" using COMSOL. We used 16000 groups to train the neural network, 2000 groups for validation, and 2000 groups for testing. In MATLAB, the validation groups are used as a threshold of the training iterations. When the mean square error within the validation groups reaches its minimum and does not decrease in the following six epoches, the training process ends. The testing groups are used to monitor the training accuracy of the DNN during the epoches. The transfer function was chosen to be a sigmoid function within the hidden layers, and the transfer function in the output layer was chosen to be a linear function. Because there are orders of magnitude difference among the input values and output values, we performed normalization for the input and output parameters to make the input and output values having the same order of magnitude. This can improve the training accuracy of the DNN.

For the seven input parameters, the range of L_{EC} and L_{EA} are both from 3 μm to 248 μm. The range of W_H is from 6 μm to 300 μm. The range of W_{EA}/W_H and W_{EAC}/W_H are both from 0.05 to 0.95. The range of $W_{EA}/W_{EA\text{-}b}$ and $W_{EC}/W_{EC\text{-}b}$ are both from 1.0 to 10.0. The DNN output, to balance the orders of different physical quantities for better performance, is a three-element normalized output vector (*SE*, *SP*, *SC*). Each element is normalized by its corresponding maximum and minimum values among the 20000 groups of dataset. For instance, the normalized *SE* is calculated by $(SE-SE_{\min})/(SE_{\max}-SE_{\min})$. The physical value is easily calculated from the normalized output value. After training with the 16000 groups, the DNN gave a testing error of 0.0013 on the 2000 testing groups. Here the testing error is the mean squared error of the normalized output vector vs the ground truth vector, as is widely used for quantifying machine learning performance and defined in MATLAB. In the following sections, we will also show comparison of DNN predicted physical *SE*, *SP*, *SC* values and the results of FEM calculations on the same inputs. The relative error of DNN results to

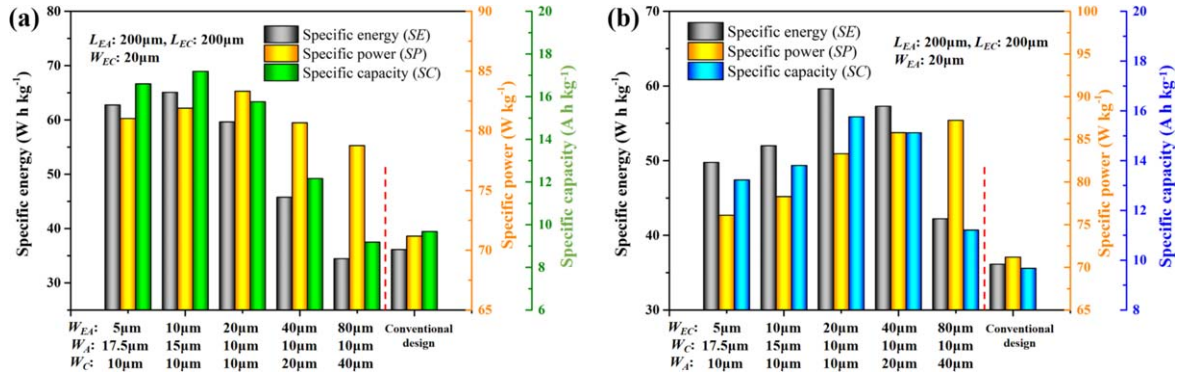

Figure 12. The cell performance with various W_{EC}/W_H and W_{EA}/W_H. (a) W_{EC} fixed at 20 μm (b) W_{EA} fixed at 20 μm.

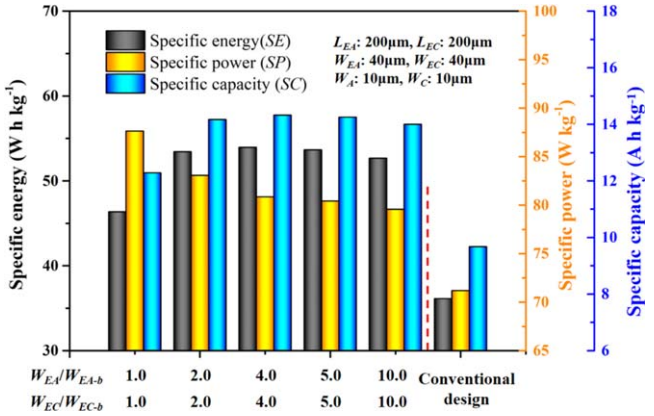

Figure 13. The cell performance with electrolyte channels of various tapering degrees.

the FEM results will provide direct indication of the DNN performance in practical applications.

Approach of design optimization.—The gradient descent algorithm was employed to optimize the electrolyte channel parameters for optimal cell performance. The trained DNN was used as a function evaluator in the optimization process. Since it is difficult to identify the concavity and convexity of the trained DNN, using the gradient descent algorithm alone may cause the algorithm to get trapped in a local optimum instead of the global optimum. We used the Markov chain Monte Carlo (MCMC) approach to address this problem. The optimization process (using the specific energy *SE* as an example) is shown in the flowchart in Fig. 16. We first generate N groups of input parameters randomly with k input parameters in each group (k =7 in this research). For the nth group at the jth iteration, the trained DNN function is first used to calculate the SE_n value. Denote the value of the ith input parameter in the nth group by $In_{n,i}^{(j)}$. The SE value is calculated by evaluating $SE(In_{n,1}^{(j)},...,In_{n,i}^{(j)},...,In_{n,k}^{(j)})$. Then the ith input parameter value is varied by a sensitive factor ε (chosen to be a very small number, 10^{-6}, which has been widely used in self-adjusting optimization processes[37–39]) to $In_{n,i}^{(j)} \cdot (1+\varepsilon)$. The trained DNN function is again used to calculate the new $SE(In_{n,1}^{(j)},...,In_{n,i}^{(j)}(1+\varepsilon),...,In_{n,k}^{(j)})$. The corresponding branch gradient, $B_{n,i}^{(j)}$, is then calculated by

$$B_{n,i}^{(j)} = \frac{SE(In_{n,1}^{(j)},...,In_{n,i}^{(j)}(1+\varepsilon),...,In_{n,k}^{(j)}) - SE(In_{n,1}^{(j)},...,In_{n,i}^{(j)},...,In_{n,k}^{(j)})}{\varepsilon}. \quad [20]$$

After calculating the branch gradients for all the k input parameters, the total gradient within this *jth* iteration is given by

$$Grad_n^{(j)} = \left| \sum_{i=1}^{k} B_{n,i}^{(j)} \right| \quad [21]$$

This total gradient is compared with 10^{-4}. If $Grad_n^{(j)}$ is less than 10^{-4}, we regard that the SE value has reached its local maximum. Then we record the local maximum SE value (denoted by SE_n) and the corresponding optimized input parameters. It should be noted that when an input parameter reaches its upper or lower bound, indicating that the bound value is the optimized value of the corresponding input parameter, the corresponding branch gradient is assigned with 0. Otherwise ($Grad_n^{(j)} \geqslant 10^{-4}$), we continue to the next iteration with the input parameters given by

$$In_{n,i}^{(j+1)} = In_{n,i}^{(j)} + \alpha\mu B_{n,i}^{(j)} \quad (i = 1, \ 2,...,k). \quad [22]$$

Here μ denotes the learning rate, which is chosen to be 0.2 in this research, and α denotes the direction adjustment factor, which is 1 when $SE(In_{n,1}^{(j+1)},...,In_{n,i}^{(j+1)}(1+\varepsilon),...,In_{n,k}^{(j+1)})$ is larger than $SE(In_{n,1}^{(j)},...,In_{n,i}^{(j)},...,In_{n,k}^{(j)})$ and -1 otherwise for finding the optimized maximum SE value. To show the window of SE, we also search for the minimum value. In finding the minimum SE, α is taken to be 1 when $SE(In_{n,1}^{(j+1)},...,In_{n,i}^{(j+1)}(1+\varepsilon),...,In_{n,k}^{(j+1)})$ is lower than $SE(In_{n,1}^{(j)},...,In_{n,i}^{(j)},...,In_{n,k}^{(j)})$ and -1 otherwise.

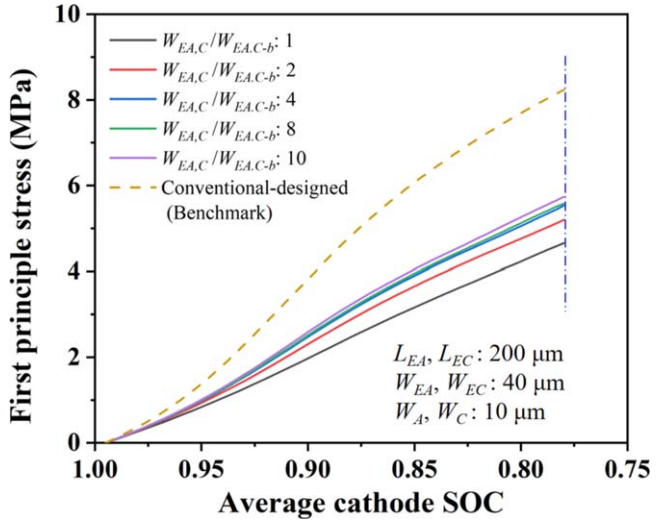

Figure 14. First principal stress in the cathode at the location of the cathode/separator interface as a function of SOC for the conventional-designed cell and cells with electrolyte channels of various tapering degrees (L_{EA}, L_{EC}: 200 μm; W_{EA}, W_{EC}: 40 μm; W_A, W_C: 10 μm).

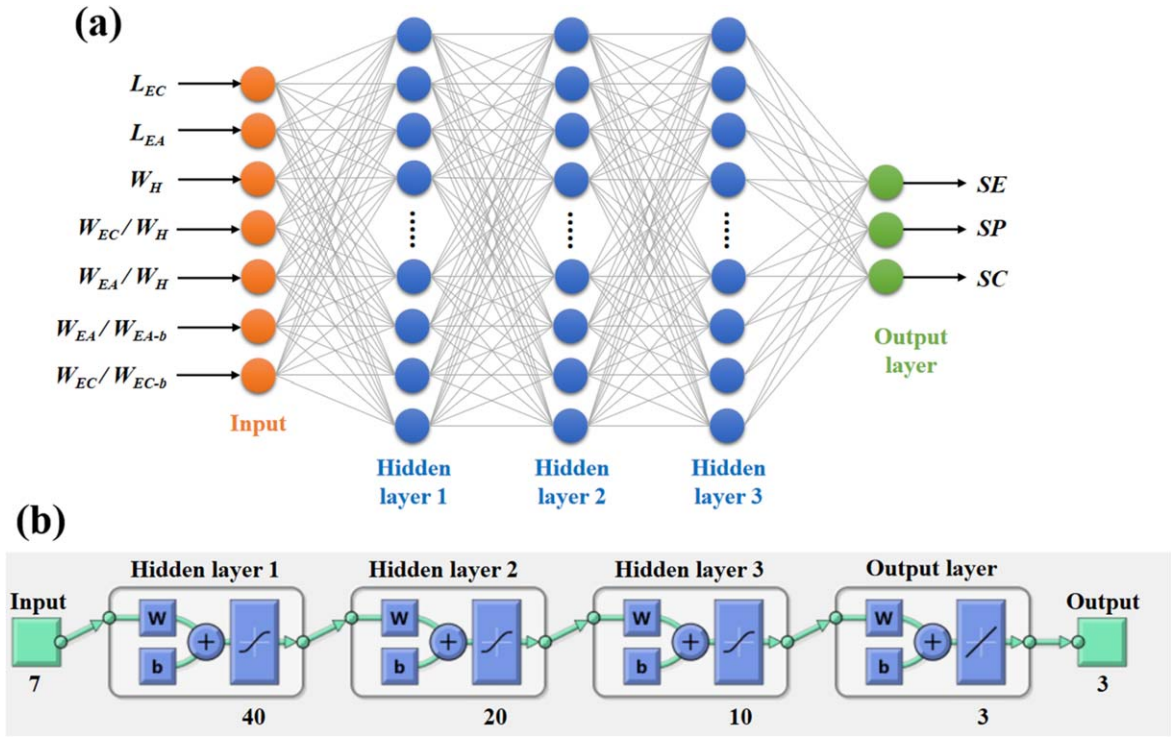

Figure 15. (a) A schematic of the machine learning system to predict cell performance with various electrolyte channel design parameters as input. (b) Set-up of the system using MATLAB.

It should be noted that for an input $In_{n,i}^{(j)}$, when $In_{n,i}^{(j+1)}$ exceeds the boundary value, we invoke the boundary-cutoff for the $j+1$ iteration by setting $B_{n,i}^{(j)}$ to be zero and $In_{n,i}^{(j+1)}$ equal to $In_{n,i}^{(j)}$.

After calculating SE_n for all the N groups of input parameters, we further check the standard deviation ratio (SDR) calculated by

$$SDR = \frac{\sqrt{\frac{1}{N}\sum_{n=1}^{N}\left(SE_n - \frac{1}{N}\sum_{n=1}^{N} SE_n\right)^2}}{\frac{1}{N}\sum_{n=1}^{N} SE_n} \quad [23]$$

If the SDR value is smaller than 10^{-2}, the maximum SE value within these N groups of SE values is regarded as the global optimized SE value, and the corresponding input parameters are regarded as the global optimized values. If the SDR value is larger than 10^{-2}, then the top 10% SE values among the N groups of SE values, and their corresponding optimized input parameters are used to form a candidate pool. A new N groups of input parameters are randomly generated, with each input parameter within the range of the upper and lower bounds of the parameters in the candidate pool. The gradient descent calculation and random generation of N groups of input parameters are repeated until the SDR value is smaller than 10^{-2}.

Design maps.—We first conducted three case studies after the DNN training to investigate the combined effect of adjusting two electrolyte channel geometrical parameters on the cell performance. The results are organized into design maps, which can provide guidance for the parametric design of the electrolyte channel geometrical parameters.

As shown in the section "Effect of electrolyte channel length", changing the cathode and anode electrolyte channel length individually can significantly affect the cell performance. Thus it is interesting to see how freely changing both the cathode and anode electrolyte channel length affects the cell performance. The ranges of L_{EA} and L_{EC} were both set to be from 5 μm to 245 μm. W_H was set to be 100 μm. W_{EA}/W_H, W_{EC}/W_H, $W_{EA}/W_{EA\text{-}b}$ and $W_{EC}/W_{EC\text{-}b}$ were set to be 0.50, 0.50, 1.5 and 1.5, respectively. The trained DNN function was utilized to calculate SE, SP and SC. The design maps are presented in Fig. 17. The maximum SE, SP and SC value was found by the MCMC gradient descent method introduced in the section "Approach of design optimization". To examine the prediction accuracy of the trained DNN, we imported the corresponding electrolyte geometrical parameter values into FEM calculations to obtain the corresponding SE, SP and SC values. The relative error, $err = |V_{i,D}\text{-}V_{i,F}|/V_{i,F}$ ($i = SE, SP, SC$), is employed to quantify the DNN accuracy where $V_{i,D}$ denotes the value calculated by DNN and $V_{i,F}$ denotes the value calculated by FEM.

The patterns of SE or SC as a function of L_{EC} and L_{EA} appears similar (Figs. 17a and 17c). Increasing L_{EC} and L_{EA} simultaneously causes SE and SC to increase. SE and SC can exceed those of the conventional-designed cell by more than 60% when L_{EC} and L_{EA} are larger than 200 μm. The maximum SE and SC values are 61.05 Wh kg^{-1} and 16.17 Ah kg^{-1}, respectively, at $L_{EC} = 230$ μm and $L_{EA} = 245$ μm. These are 69.07% and 67.22% larger than the SE and SC of the conventional-designed cell (SE: 36.11 Wh kg^{-1}, SC: 9.67 Ah kg^{-1}), respectively. With increasing L_{EA} and L_{EC}, SP increases monotonically (Fig. 17b), indicating that increasing cathode and anode electrolyte channel length can continuously increase the specific power. The maximum SP (84.08 W kg^{-1}) is reached when L_{EA} and L_{EC} are both 245 μm. This SP value is 18.14% larger than that of the conventional-designed cell (71.17 W kg^{-1}). It can also be seen that changing the cathode electrolyte channel length has a stronger effect on the cell performance.

We further created the Ragone plane for showing the window of all possible specific energy and specific power of the cell with changing L_{EC} and L_{EA} based on DNN and MCMC. It can be seen from Fig. 17d that when SE is relatively small (below 47.50 Wh kg^{-1}), the SP span is narrow. The difference between the maximum and minimum SP is approximately 0.6 W kg^{-1} under a constant SE value. When SE is within 47.50 Wh kg^{-1} and

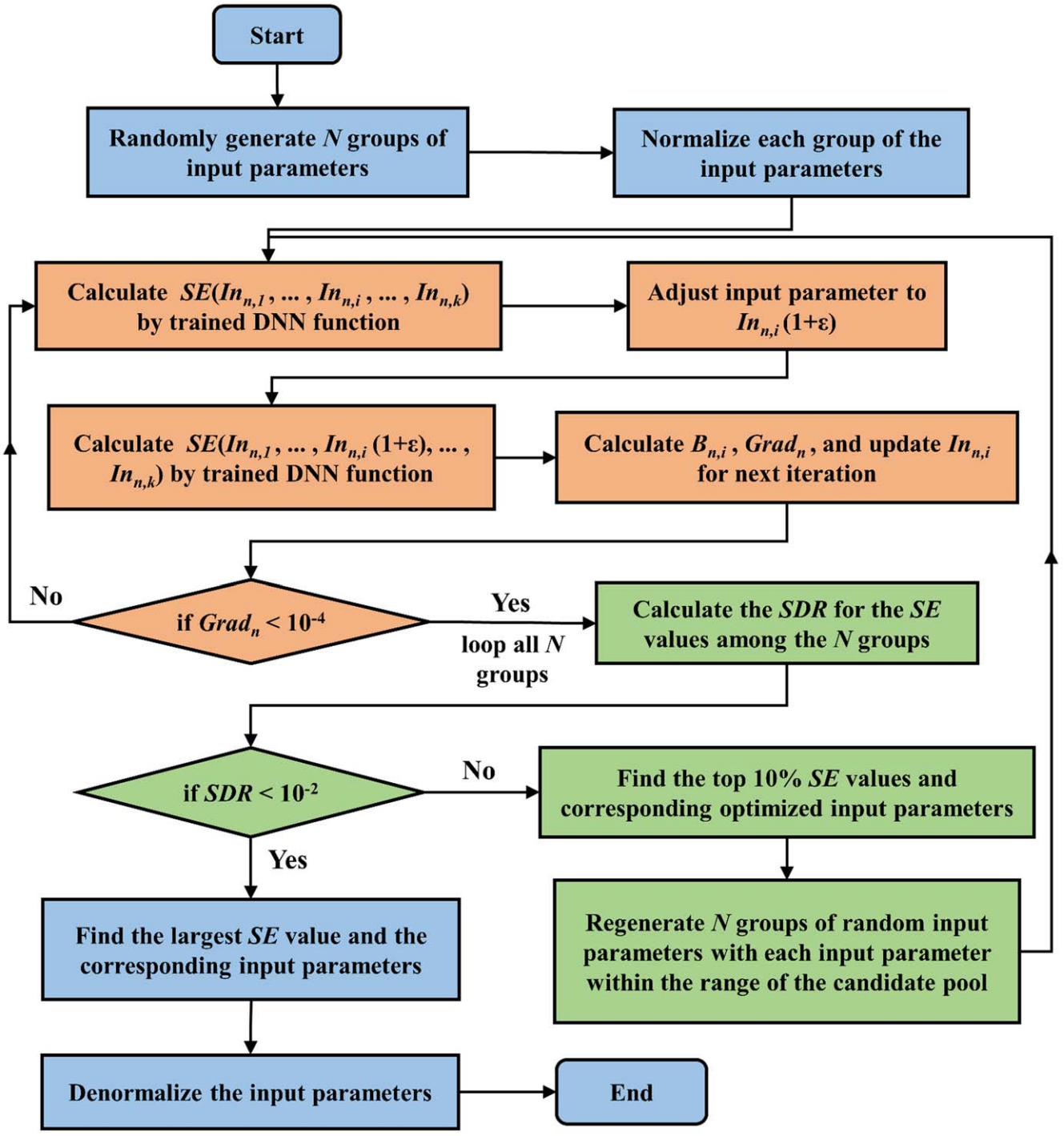

Figure 16. Flow chart showing the optimization process (for finding the maximum specific energy as an example) based on the MCMC gradient descent method.

54.80 W kg^{-1}, the upper bound of *SP* increases sharply with *SE*, while the slope of the lower bound of *SP* does not change significantly. This causes the span of *SP* to increase with *SE*. The maximum *SP* span reaches 4.5 W kg^{-1} as *SE* reaches 54.80 Wh kg^{-1}. When *SE* is within 54.80 Wh kg^{-1} and 61.05 Wh kg^{-1}, the slope of the upper bound of *SP* decreases, while the slope of the lower bound of *SP* increases. Eventually, the *SP* span reduces to zero when *SE* reaches its maximum. We selected 34 data points at the upper and low bounds obtained by DNN and MCMC, extracted the corresponding seven electrolyte channel input parameters for each of the data point, and input them into FEM calculations. The FEM results are shown as circles. It is seen that the *SE* and *SP* values predicted by DNN and those by FEM agree very well. The average of the relative error of the 34 points are 1.08% for *SE* and 0.17% for *SP*, indicating that the DNN has a high accuracy. Finally, it can be seen from Figs. 17e that using the electrolyte channel geometrical parameters corresponding to the maximum *SE*, *SP* and *SC*, the values calculated by DNN are very close to those calculated by FEM simulations. The relative errors are all far below 5%, again indicating that the accuracy of the trained DNN is high enough for conducting this first case study.

Figure 18 shows the design maps of changing cathode and anode electrolyte channel width as the second case study. The ranges of W_{EA}/W_H and W_{EC}/W_H were both chosen to be from 0.05 to 0.95. L_{EA} and L_{EC} were both set to be 200 μm. W_H was set to be 100 μm. $W_{EC}/W_{EC\text{-}b}$ and $W_{EA}/W_{EA\text{-}b}$ were both set to be 1.5. The maximum

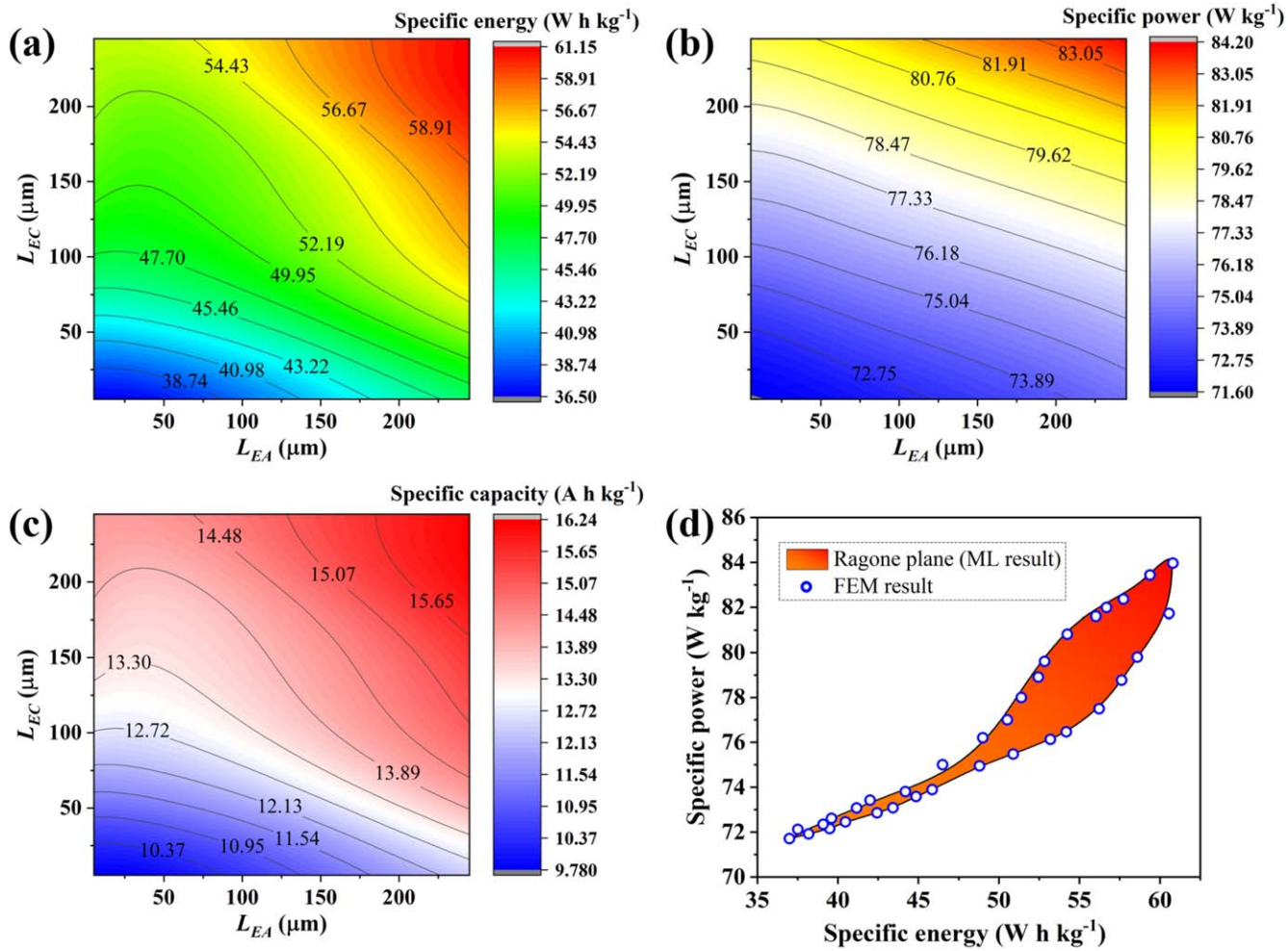

(e) Maximum values

Item	ML result	FEM result	Error
SE	61.05 W h kg^{-1}	60.17 W h kg^{-1}	1.46%
SP	84.08 W kg^{-1}	83.62 W kg^{-1}	0.55%
SC	16.17 A h kg^{-1}	16.18 A h kg^{-1}	0.06%

Figure 17. Design maps and the Ragone plane for the cell performance by freely changing both cathode and anode electrolyte channel lengths. (a) The contour of specific energy. (b) The contour of specific power. (c) The contour of specific capacity. (d) The Ragone plane acquired by DNN machine learning (ML) and MCMC showing the window of all possible *SE* and *SP* with changing L_{EA} and L_{EC}. The FEM simulation results show that DNN accurately captures the bound values. (e) The maximum *SE*, *SP* and *SC* calculated by DNN on their corresponding optimized geometrical parameters found by the DNN and MCMC method, and the FEM results calculated on the same corresponding electrolyte channel geometrical parameters. The comparison shows the DNN accuracy. (W_H: 100 μm, W_{EA}/W_H: 0.5, W_{EC}/W_H: 0.5, $W_{EA}/W_{EA\text{-}b}$: 1.5, $W_{EC}/W_{EC\text{-}b}$: 1.5).

SE, *SP* and *SC* were found by the MCMC gradient descent method. To examine the prediction accuracy of the trained DNN, we imported the corresponding electrolyte geometrical parameter values into FEM calculations to obtain the corresponding *SE*, *SP* and *SC* values. The relative error is employed to quantify the DNN accuracy.

The patterns of *SE* or *SC* as a function of cathode and anode electrolyte channel width appear similar (Figs. 18a and 18c). *SE* and *SC* both first increase and then decrease with W_{EA}/W_H and W_{EC}/W_H, and show a peak in the middle region of map. When W_{EA}/W_H is in the range of 0.20 to 0.45 and W_{EC}/W_H is in the range of 0.50 to 0.65, the cell shows more than 65% increase in specific energy and specific capacity than the conventional-designed cell. The maximum *SE* and *SC* are 62.17 Wh kg^{-1} and 16.46 Ah kg^{-1} when W_{EA}/W_H and W_{EC}/W_H are 0.33 and 0.54, respectively. These are 72.17% and 70.22% higher than the *SE* and *SC* of the conventional-designed cell, respectively. It can also be seen that when W_{EA}/W_H and W_{EC}/W_H are approximately above 0.84 and 0.92, respectively, *SE* and *SC* are lower than those of the conventional-designed cell. These indicate that changing the cathode and anode electrolyte width can significantly influence both the specific energy and specific capacity. However, inappropriate design of the electrolyte channel width may reduce the cell performance. *SP* increases almost monotonically with W_{EA}/W_H and W_{EC}/W_H (Fig. 18b), indicating that increasing cathode or anode electrolyte channel width can continuously increase the specific power. The maximum *SP* is 90.75 W kg^{-1} when W_{EA}/W_H and W_{EC}/W_H are 0.80 and 0.95, respectively. This is 27.52% larger

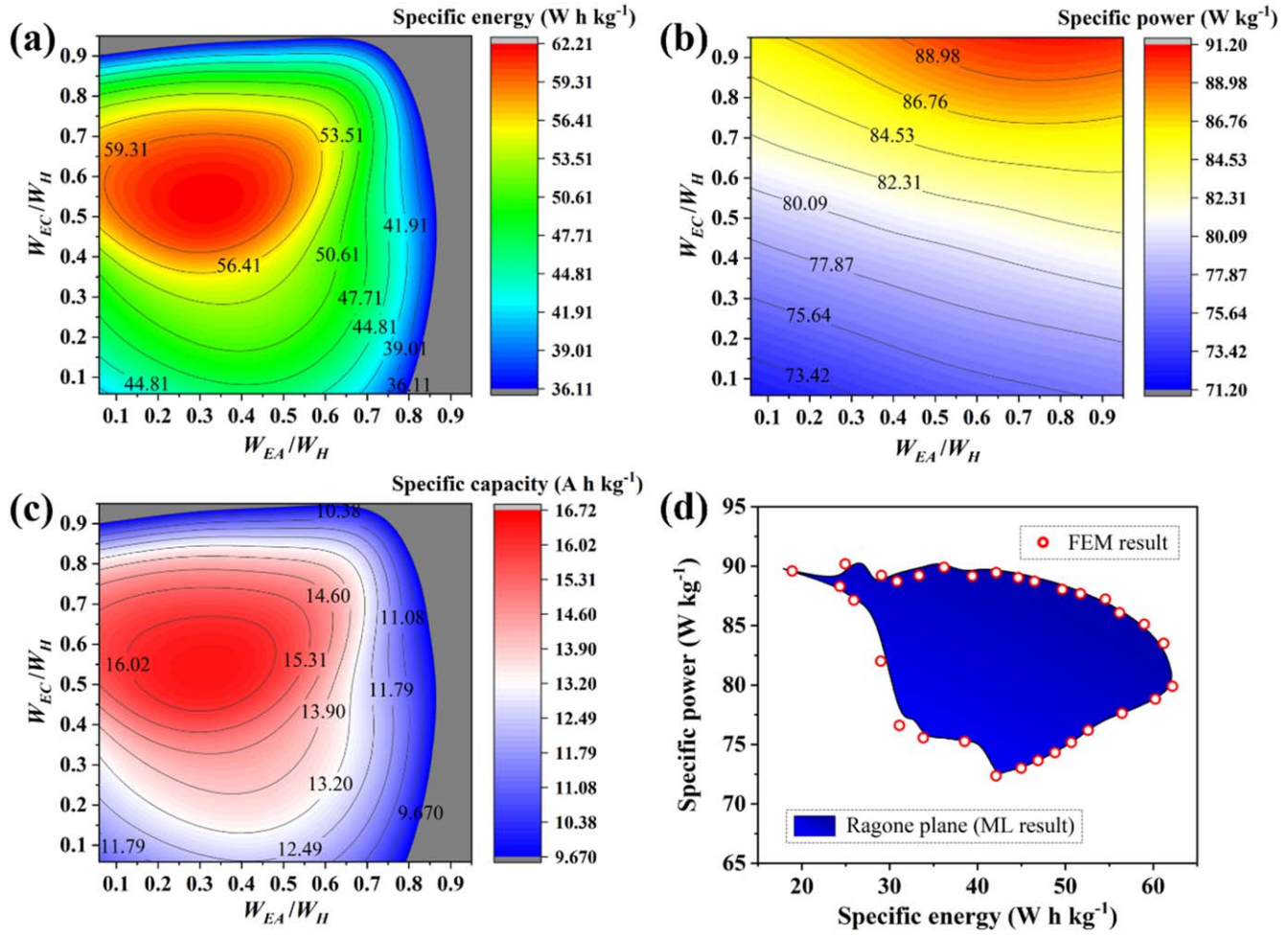

(e) Maximum values

Item	ML result	FEM result	Error
SE	62.17 W h kg^{-1}	62.43 W h kg^{-1}	0.42%
SP	90.75 W kg^{-1}	89.67 W kg^{-1}	1.20%
SC	16.46 A h kg^{-1}	16.54 A h kg^{-1}	0.48%

Figure 18. Design maps and Ragone plane for the cell performance by freely changing both cathode and anode electrolyte channel widths. (a) The contour of specific energy. (b) The contour of specific power. (c) The contour of specific capacity. (d) The Ragone plane acquired by DNN machine learning (ML) and MCMC showing the window of all possible *SE* and *SP* with changing W_{EA}/W_H and W_{EC}/W_H. The FEM simulation results show that DNN accurately captures the bound values. (e) The maximum *SE*, *SP* and *SC* calculated by DNN on their corresponding optimized geometrical parameters found by the DNN and MCMC method, and the FEM results calculated on the same corresponding electrolyte channel geometrical parameters. The comparison shows the DNN accuracy. (L_{EC}: 200 μm, L_{EA}: 200 μm, W_H: 100 μm, $W_{EA}/W_{EA\text{-}b}$: 1.5, $W_{EC}/W_{EC\text{-}b}$: 1.5; The gray area indicates the regions where the cell performance is lower than that of the conventional-designed cell).

than the *SP* of the conventional-designed cell. Changing the cathode electrolyte channel width has a stronger effect on *SP* than changing the anode electrolyte channel width.

We further created the Ragone plane for showing the window of all possible specific energy and specific power of the cell with changing W_{EA}/W_H and W_{EC}/W_H by DNN and MCMC. It is seen from Fig. 18d that as *SE* increases from 17.90 Wh kg^{-1} to 42.00 Wh kg^{-1}, the upper bound of *SP* shows two increase-decrease curves with *SE*. The lower bound of *SP* decreases sharply and then more slowly. These cause the *SP* span to show a bird head shape. When *SE* is within 42.00 Wh kg^{-1} and 62.17 Wh kg^{-1}, the upper bound of *SP* decreases gradually, while the lower bound of *SP* increases almost linearly with *SE*. Eventually, the *SP* span reduces to zero when *SE* reaches its maximum. We selected 31 data points at the upper and low bounds obtained by DNN and MCMC, extracted the corresponding seven electrolyte channel input parameters for each of the data point, and input them into FEM calculations. The FEM results are shown as circles. It is seen that the *SE* and *SP* values predicted by DNN and those by FEM agree very well. The average of the relative error of the 31 points are 3.86% for *SE* and 0.65% for *SP*. The average of the relative error is 1.41% for *SE* and 0.64% for *SP* when *SE* is larger than 40 Wh kg^{-1}. These indicate that the DNN has a high accuracy. Finally, it can be seen in Fig. 18e that the errors of the maximum *SE*, *SP* and *SC* calculated by DNN are all far below 5%,

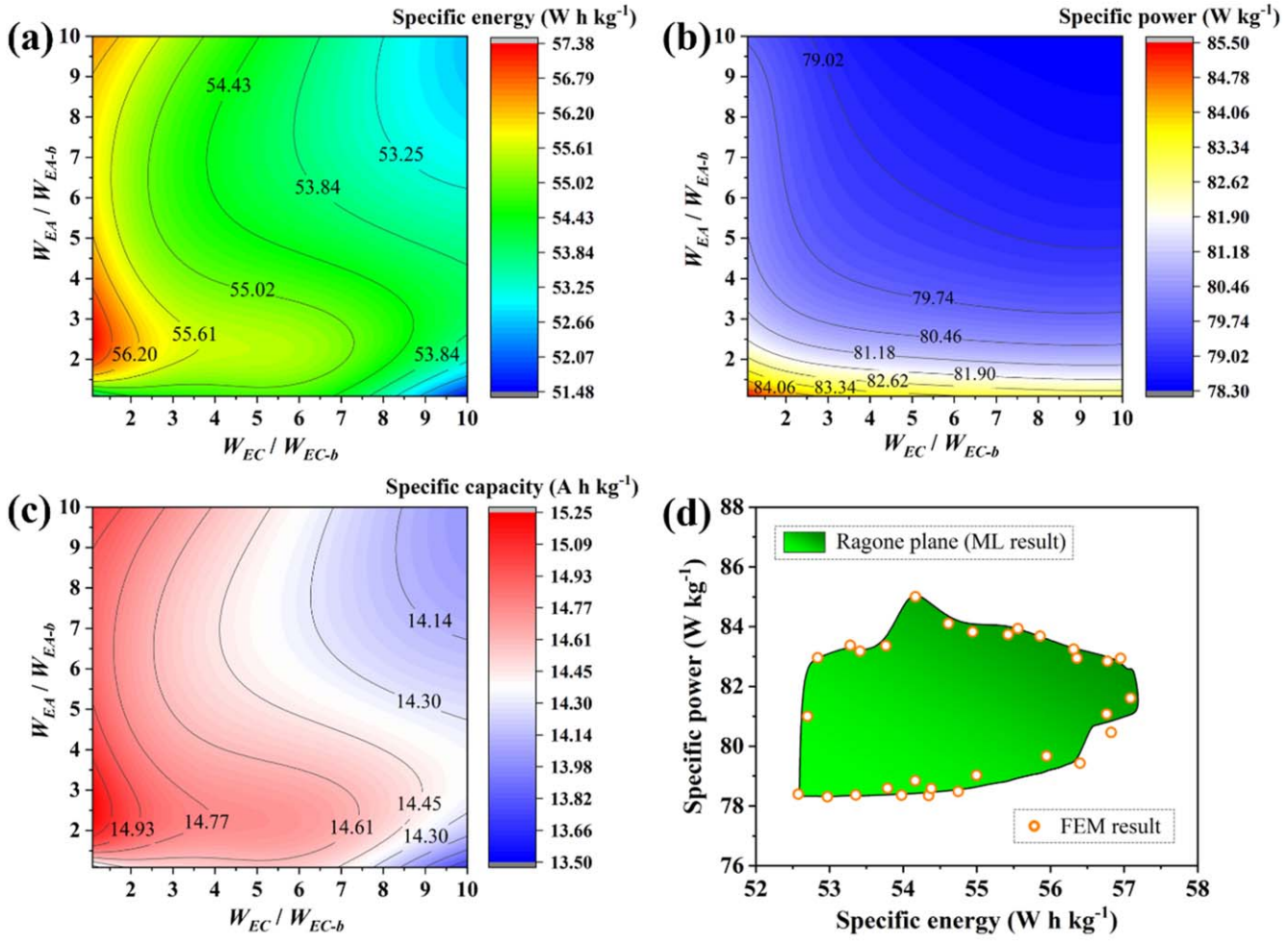

(e) Maximum values

Item	ML result	FEM result	Error
SE	57.32 W h kg^{-1}	55.89 W h kg^{-1}	2.56%
SP	85.02 W kg^{-1}	85.79 W kg^{-1}	0.90%
SC	15.22 A h kg^{-1}	14.93 A h kg^{-1}	1.94%

Figure 19. Design maps and Ragone plane for the cell performance by freely changing both cathode and anode electrolyte channel tapering degrees. (a) The contour of specific energy. (b) The contour of specific power. (c) The contour of specific capacity. (d) The Ragone plane acquired by DNN machine learning (ML) and MCMC showing the window of all possible *SE* and *SP* with changing $W_{EA}/W_{EA\text{-}b}$ and $W_{EC}/W_{EC\text{-}b}$. The FEM simulation results show that DNN accurately captures the bound values. (e) The maximum *SE*, *SP* and *SC* calculated by DNN on their corresponding optimized geometrical parameters found by the DNN and MCMC method, and the FEM results calculated on the same corresponding electrolyte channel geometrical parameters. The comparison shows the DNN accuracy. (L_{EC}: 200 μm, L_{EA}: 200 μm, W_H: 100 μm, W_{EA}/W_H: 0.6, W_{EC}/W_H: 0.6).

again indicating that the trained DNN has a high enough accuracy in conducting this second case study.

Figure 19 shows the design maps of changing cathode and anode electrolyte channel tapering degree as the third case study. The ranges of $W_{EA}/W_{EA\text{-}b}$ and $W_{EC}/W_{EC\text{-}b}$ were both set to be from 1.0 to 10.0. L_{EA} and L_{EC} were both set to be 200 μm. W_H was set to be 100 μm. W_{EA}/W_H and W_{EC}/W_H were both set to be 0.60.

As can be seen in Figs. 19a and 19c, the patterns of *SE* or *SC* as a function of cathode and anode electrolyte channel tapering degree appear similar. When $W_{EC}/W_{EC\text{-}b}$ is below 1.5 and $W_{EA}/W_{EA\text{-}b}$ is between 2.0 and 3.4, the specific energy and specific capacity are improved for more than 55% compared with the conventional-designed cell. The maximum *SE* and *SC* are 57.32 Wh kg^{-1} and 15.22 Ah kg^{-1} when $W_{EC}/W_{EC\text{-}b}$ and $W_{EA}/W_{EA\text{-}b}$ are 1.0 and 2.5, respectively. These are 58.74% and 57.40% larger than the *SE* and *SC* of the conventional-designed cell, respectively. *SP* decreases monotonically with $W_{EC}/W_{EC\text{-}b}$ and $W_{EA}/W_{EA\text{-}b}$. When $W_{EC}/W_{EC\text{-}b}$ and $W_{EA}/W_{EA\text{-}b}$ are both above 3.5, any increase of $W_{EC}/W_{EC\text{-}b}$ and $W_{EA}/W_{EA\text{-}b}$ does not affect *SP* much.

We further created the Ragone plane for showing the window of all possible specific energy and specific power of the cell with changing cathode and anode electrolyte channel tapering degree based on DNN and MCMC. It can be seen from Fig. 19d that the lower bound of *SP* increases monotonically with *SE*. The upper bound of *SP* first increases (except a minor dip) till 85.02 W kg^{-1} as *SE* increases from 52.79 Wh kg^{-1} to 54.15 Wh kg^{-1}, and then

decreases gradually with some minor fluctuations as *SE* increases from 54.15 Wh kg^{-1} to 57.32 Wh kg^{-1}. These cause the *SP* span to have a relatively large value initially and then decrease slowly after *SE* reaches 55.50 Wh kg^{-1}. We selected 30 data points at the upper and low bounds obtained by DNN and MCMC, extracted the corresponding seven electrolyte channel input parameters for each of the data point, and input them into FEM calculations. The FEM results are shown as circles. It is seen that the *SE* and *SP* values predicted by DNN and those by FEM agree well. The average of the relative error of the 30 points are 1.46% for *SE* and 0.38% for *SP*, indicating that the DNN has a high accuracy. Finally, it can be seen in Fig. 19e that the errors of the maximum *SE*, *SP* and *SC* calculated by DNN are all far below 5%, again indicating that the trained DNN has a high enough accuracy in conducting this third case study.

Optimal design by freely changing 6 geometrical parameters.— The design maps in the previous section shows that by freely changing two electrolyte channel geometrical parameters, the cell performance can be significantly improved. The optimized specific energy, specific power, and specific capacity are much higher than those of the conventional-designed cell. In this section, more freely changeable electrolyte channel geometrical parameters are taken into consideration to further explore the potential of performance improvement. W_H was kept to be constant at 100 μm. The other electrolyte channel geometrical parameters were all set to be variable. The range of L_{EA} and L_{EC} were both from 5 μm to 245 μm. The range of W_{EA}/W_H and W_{EC}/W_H were both set to be from 0.05 to 0.95. The range of $W_{EA}/W_{EA\text{-}b}$ and $W_{EC}/W_{EC\text{-}b}$ were both set to be from 1.0 to 10.0. The MCMC gradient descent was utilized to find the global optimized values. The specific energy was chosen to be the optimization goal. After optimization, the maximum *SE* value was 64.54 Wh kg^{-1}, which is 78.73% larger than that of the conventional-designed cell (36.11 Wh kg^{-1}). The corresponding optimized L_{EA}, L_{EC}, W_{EA}/W_H, W_{EC}/W_H, $W_{EA}/W_{EA\text{-}b}$ and $W_{EC}/W_{EC\text{-}b}$ values were 240.00 μm, 231.40 μm, 0.3313, 0.7496, 1.05 and 9.18 respectively, indicating that changing 6 electrolyte channel geometrical parameters can give even larger specific energy than adjusting only 2 geometrical parameters. The results again indicate that with the introduction of bio-inspired electrolyte channels inside the thick electrode, the battery performance can be significantly improved during fast charging. Finally, FEM calculations were employed to examine the accuracy of the optimized *SE*. Using the corresponding optimized electrolyte channel parameters, the FEM calculation gave *SE* to be 66.02 Wh kg^{-1}. The relative error is only 2.24%, which is below the typical engineering requirement of 5%. This suggests that the trained DNN has a high enough accuracy for conducting the optimization.

Conclusions

In this research, we introduced a bio-inspired Li-ion battery cell design strategy by adding electrolyte channels inside the thick electrode and investigated the effect of electrolyte channel geometrical parameters on the electrochemical performance and mechanical integrity of battery cells during fast charging. First, the impact of electrolyte channel length, width, tapering degree, and active electrode material width on cell performance were investigated. Then, a DNN machine learning system was built to correlate the electrolyte geometrical parameters and cell performance. The MCMC method was applied for optimization. Finally, we obtained three groups of design maps and demonstrated optimization of specific energy with 6 freely adjustable electrolyte channel geometrical parameters. The conclusions are summarized below

(1) Changing the electrolyte channel geometry causes the battery cell performance, including specific energy, specific power, and specific capacity, to vary significantly. The performance can be greatly improved comparing to the conventional-designed cell. On the other hand, inappropriate design can decrease the performance. The local state of charge of the electrode during CC charging can also be significantly affected by the electrolyte channel geometrical parameters.

(2) During charging, the cathode material undergoes tensile stress, while the anode material undergoes compressive stress. The stress level in the cathode is larger. The maximum first principal stress in the cathode occurs at the location of cathode/separator interface. With electrolyte channel design, the maximum first principal stress can be significantly reduced comparing to that of the conventional-designed cell.

(3) After training, the developed DNN machine learning system can correlate the electrolyte geometrical parameters with the battery performance with a high accuracy, which can assist the parametric design of electrolyte channels. The MCMC gradient descent method and the trained DNN evaluation function have provided optimized solution without the need to know the concavity or convexity of the DNN function. The accuracy of the predicted optimized solution such as specific energy has been confirmed by FEM simulations.

(4) The design maps show that the pattern of specific energy on electrolyte channel geometrical parameters (cathode and anode electrolyte channel length, width, tapering degree) appears similar to the pattern of specific capacity on these parameters. The specific power increases almost monotonically with these parameters. By freely changing two electrolyte channel geometrical parameters, the specific energy and specific capacity can both be improved by more than 70%, while the specific power can be improved by more than 20%. By freely changing six electrolyte channel geometrical parameters, even more cell performance improvement can be achieved. The optimized specific energy is 78.73% larger than that of the conventional-designed cell. All these suggest that the introduction of bio-inspired electrolyte channel with appropriate geometrical parameters inside the thick electrode can bring great performance improvement.

Lithium plating can occur when the charging current density is very high such that the anode over-potential is below 0 V vs Li^+/Li. Lithium plating is more likely to happen on a thick electrode at the anode/separator interface because of the slow lithium ion transport through the thick electrode toward the interior of the anode next to the anode/current collector interface. While lithium plating is outside the scope of this paper, we would like to highlight that a key benefit of electrolyte channels is to enhance lithium ion transport. These channels can facilitate lithium ion transport toward the interior of the anode, reducing the possible accumulation of lithium ions at the anode surface next to the separator. As a result, electrolyte channels can potentially help to significantly reduce lithium plating. Using channel structures in an electrode to reduce lithium plating is an interesting topic for further study.

Acknowledgments

The authors gratefully acknowledge the support by the National Science Foundation under grant no. CNS-1446117 and by LG Chem.

Appendix A: The parameters used in this research

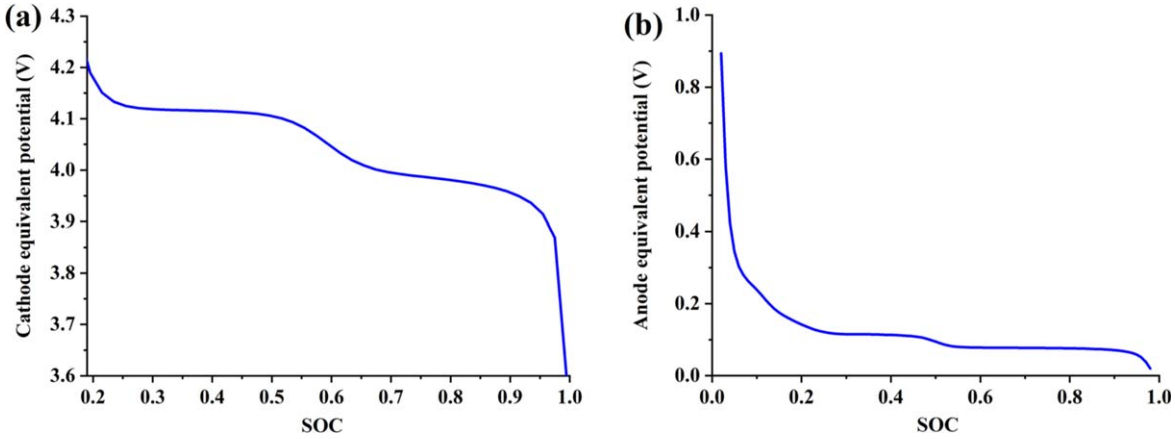

Figure A·1. (a) The equilibrium potential of the cathode material ($Li_yMn_2O_4$). (b) The equilibrium potential of the anode material (Li_xC_6).

Table A·I. The electrochemical and mechanical parameters used in this research.[23,25,30,31]

Parameter	Symbol	Value
α	Anodic charge transfer coefficient	0.5
$c_{s,\max}$ (anode)	Maximum lithium concentration in anode particle	31507 mol m^{-3}
$c_{s,\max}$ (cathode)	Maximum lithium concentration in cathode particle	22860 mol m^{-3}
D_{e0}	Diffusivity of lithium ion in bulk electrolyte	curve (see Ref. 32)
D_s (anode)	Diffusivity of lithium ion in anode particle	1.45×10^{-13} m^2 s^{-1}
D_s (cathode)	Diffusivity of lithium ion in cathode particle	1×10^{-14} m^2 s^{-1}
E_p (anode)	Young's modulus of the solid particle (anode)	768.3 MPa
E_p (cathode)	Young's modulus of the solid particle (cathode)	733.1 MPa
F	Faraday constant	96485 C mol^{-1}
k	Reaction rate constant for cathode and anode active material	2×10^{-11} $m^{2.5}$ $mol^{-2.5}$ s^{-1}
r_p	Cathode and anode particle radius	5 μm
R	Gas constant	8.3145 J mol^{-1} K^{-1}
t_+	Lithium ion transference number	curve (see Ref. 32)
T	Temperature	298 K
ε_b	Electrode binding material volume fraction	0.10
ε_e (anode)	Electrolyte volume fraction (anode)	0.48
ε_e (cathode)	Electrolyte volume fraction (cathode)	0.45
ε_e (separator)	Electrolyte volume fraction (separator)	0.39
ε_s (anode)	Solid phase volume fraction (anode)	0.42
ε_s (cathode)	Solid phase volume fraction (cathode)	0.45
ε_{sep}	Separator solid phase volume fraction	0.61
κ_{e0}	Bulk electrolyte conductivity	curve (see Ref. 32)
ν_p (anode)	Poisson's ratio of the solid particle (anode)	0.14
ν_p (cathode)	Poisson's ratio of the solid particle (cathode)	0.15
ρ_{Al}	Aluminum current collector density	2707 kg m^{-3}
ρ_b	Electrode binding material density	1800 kg m^{-3}
ρ_{Cu}	Copper current collector density	8954 kg m^{-3}
ρ_e	Electrolyte density	1324 kg m^{-3}
ρ_{Grap}	Anode active material density (graphite)	2200 kg m^{-3}
ρ_{LMO}	Cathode active material density (LMO)	4210 kg m^{-3}
ρ_{sep}	Separator material density	855 kg m^{-3}
σ_{s0} (anode)	Anode solid electronic conductivity	100 s m^{-1}
σ_{s0} (cathode)	Cathode solid electronic conductivity	3.8 s m^{-1}
Ω (anode)	Lithium ion partial molar volume (graphite anode)	3.646×10^{-6} m^3 mol^{-1}
Ω (cathode)	Lithium ion partial molar volume (LMO cathode)	3.497×10^{-6} m^3 mol^{-1}

ORCID

Wei Lu https://orcid.org/0000-0002-4851-1032

References

1. L. Lu, X. Han, J. Li, J. Hua, and M. Ouyang, "A review on the key issues for lithium-ion battery management in electric vehicles." *J. Power Sources*, **226**, 272 (2013).
2. T. Gao and W. Lu, "Electrochimica acta mechanism and effect of thermal degradation on electrolyte ionic diffusivity in li-ion batteries : a molecular dynamics study." *Electrochim. Acta*, **323**, 134791 (2019).
3. Y. Kuang, C. Chen, D. Kirsch, and L. Hu, "Thick electrode batteries: principles, opportunities, and challenges." *Adv. Energy Mater.*, **9**, 1901457 (2019).
4. Zhijia Du, D. L. Wood III, C. Daniel, S. Kalnaus, and Jianlin Li, "Understanding limiting factors in thick electrode performance as applied to high energy density Li-ion batteries." *J. Appl. Electrochem.*, **47**, 405 (2017).

5. J. Billaud, F. Bouville, T. Magrini, C. Villevieille, and A. R. Studart, "Magnetically aligned graphite electrodes for high-rate performance Li-ion batteries." *Nat. Energy*, **1**, 1 (2016).
6. V. Zadin, D. Brandell, H. Kasemägi, A. Aabloo, and J. O. Thomas, "Finite element modelling of ion transport in the electrolyte of a 3D-microbattery." *Solid State Ionics*, **192**, 279 (2011).
7. V. Zadin, H. Kasemägi, A. Aabloo, and D. Brandell, "Modelling electrode material utilization in the trench model 3D-microbattery by finite element analysis." *J. Power Sources*, **195**, 6218 (2010).
8. K. Sun, T. Wei, B. Y. Ahn, J. Y. Seo, S. J. Dillon, and J. A. Lewis, "3D printing of interdigitated li-ion microbattery architectures." *Adv. Mater.*, **25**, 4539 (2013).
9. B. Dunn, J. W. Long, and D. R. Rolison, "Rethinking multifunction in three dimensions for miniaturizing electrical energy storage." *Electrochem. Soc. Interface*, **17**, 49 (2008).
10. R. W. Hart, H. S. White, B. Dunn, and D. R. Rolison, "3-D Microbatteries." *Electrochem. commun.*, **5**, 120 (2003).
11. C. Bae, C. K. Erdonmez, J. W. Halloran, and Y. Chiang, "Design of battery electrodes with dual-scale porosity to minimize tortuosity and maximize performance." *Adv. Mater.*, **25**, 1254 (2013).
12. C. Chen, Y. Zhang, Y. Li, Y. Kuang, J. Song, W. Luo, and Y. Wang, "Highly Conductive, Lightweight, Low-Tortuosity Carbon Frameworks as Ultrathick 3D Current Collectors." *Adv. Energy Mater.*, **7**, 1700595 (2017).
13. V. P. Nemani, S. J. Harris, and K. C. Smith, "Design of Bi-tortuous, anisotropic graphite anodes for fast ion-transport in li-ion batteries." *J. Electrochem. Soc.*, **162**, A1415 (2015).
14. Y. Kim, A. Drews, R. Chandrasekaran, T. Miller, and J. Sakamoto, "Improving Li-ion battery charge rate acceptance through highly ordered hierarchical electrode design." *Ionics*, **24**, 2935 (2018).
15. T. Hutzenlaub, A. Asthana, J. Becker, D. R. Wheeler, R. Zengerle, and S. Thiele, "Electrochemistry communications FIB/SEM-based calculation of tortuosity in a porous LiCoO 2 cathode for a Li-ion battery." *Electrochem. Commun.*, **27**, 77 (2013).
16. J. Landesfeind, J. Hattendorff, A. Ehrl, W. A. Wall, and H. A. Gasteiger, "Tortuosity determination of battery electrodes and separators by impedance spectroscopy." *J. Electrochem. Soc.*, **163**, A1373 (2016).
17. G. Ye, W. Tong, X. Liu, X. Song, J. Zhou, and X. Zhou, "Chemical engineering research and design an analytical method for the optimization of pore network in lithium-ion battery electrodes." *Chem. Eng. Res. Des.*, **149**, 226 (2019).
18. T. M. Clancy and J. F. Rohan, "Simulations of 3D nanoscale architectures and electrolyte characteristics for Li-ion microbatteries." *J. Energy Storage.*, **23**, 1 (2019).
19. E. R. Reale and K. C. Smith, "Capacitive performance and tortuosity of activated carbon electrodes with macroscopic pores." *J. Electrochem. Soc.*, **165**, A1685 (2018).
20. J. Li, X. Liang, R. Panat, and J. Park, "Enhanced battery performance through three-dimensional structured electrodes : experimental and modeling study." *J. Electrochem. Soc.*, **165**, A3566 (2018).
21. M. Doyle, T. F. Fuller, and J. Newman, "Modeling of galvanostatic charge and discharge of the lithium/polymer/insertion cell." *J. Electrochem. Soc.*, **140**, 1526 (1993).
22. L. Liu, J. Park, X. Lin, A. M. Sastry, and W. Lu, "A thermal-electrochemical model that gives spatial-dependent growth of solid electrolyte interphase in a Li-ion battery." *J. Power Sources*, **268**, 482 (2014).
23. X. Lin, J. Park, L. Liu, Y. Lee, A. M. Sastry, and W. Lu, "A comprehensive capacity fade model and analysis for li-ion batteries." *J. Electrochem. Soc.*, **160**, A1701 (2013).
24. X. Lin and W. Lu, "A framework for optimization on battery cycle life." *J. Electrochem. Soc.*, **165**, A3380 (2018).
25. B. Wu, S. Han, K. G. Shin, and W. Lu, "Application of artificial neural networks in design of lithium-ion batteries." *J. Power Sources*, **395**, 128 (2018).
26. X. Dang, L. Yan, K. Xu, X. Wu, H. Jiang, and H. Sun, "Electrochimica acta open-circuit voltage-based state of charge estimation of lithium-ion battery using dual neural network fusion battery model." *Electrochim. Acta*, **188**, 356 (2016).
27. T. Weigert, Q. Tian, and K. Lian, "State-of-charge prediction of batteries and battery – supercapacitor hybrids using artificial neural networks." *J. Power Sources*, **196**, 4061 (2011).
28. Y. Takagishi, T. Yamanaka, and T. Yamaue, "Machine learning approaches for designing meso-scale structure of li-ion battery electrodes." *Batteries*, **5**, 54 (2019).
29. T. Parthiban, R. Ravi, and N. Kalaiselvi, "Exploration of artificial neural network [ANN] to predict the electrochemical characteristics of lithium-ion cells." *Electrochim. Acta*, **53**, 1877 (2007).
30. B. Wu and W. Lu, "A battery model that fully couples mechanics and electrochemistry at both particle and electrode levels by incorporation of particle interaction." *J. Power Sources*, **360**, 360 (2017).
31. S. Lee, J. Yang, and W. Lu, "Debonding at the interface between active particles and PVDF binder in Li-ion batteries." *Extrem. Mech. Lett.*, **6**, 37 (2016).
32. H. Lundgren, M. Behm, and G. Lindbergh, "Electrochemical characterization and temperature dependency of mass-transport properties of LiPF 6 in EC : DEC." *J. Electrochem. Soc.*, **162**, A413 (2015).
33. X. Zhang, W. Shyy, and A. M. Sastry, "Numerical Simulation of Intercalation-Induced Stress in Li-Ion battery electrode particles." *J. Electrochem. Soc.*, **154**, A910 (2007).
34. A. P. Roberts and E. J. Garboczi, "Elastic properties of model porous ceramics." *J. Am. Ceram. Soc.*, **83**, 3041 (2000).
35. Y. Abe and S. Kumagai, "Effect of negative/positive capacity ratio on the rate and cycling performances of LiFePO4/graphite lithium-ion batteries." *J. Energy Storage.*, **19**, 96 (2018).
36. C. S. Kim, K. M. Jeong, K. Kim, and C. W. Yi, "Effects of capacity ratios between anode and cathode on electrochemical properties for lithium polymer batteries." *Electrochim. Acta*, **155**, 431 (2015).
37. T. Gao, L. Ying, M. Dai, G. Shen, P. Hu, and L. Shen, "International Journal of thermal sciences a comparative study of temperature-dependent interfacial heat transfer coe ffi cient prediction methods for 22MnB5 steel in spray quenching process." *Int. J. Therm. Sci.*, **139**, 36 (2019).
38. L. Ying, T. Gao, M. Dai, and P. Hu, "Investigation of interfacial heat transfer mechanism for 7075-T6 aluminum alloy in HFQ hot forming process." *Appl. Therm. Eng.*, **118**, 266 (2017).
39. L. Ying, T. Gao, M. Dai, Y. Yang, and P. Hu, "Experimental investigation of temperature-dependent interfacial heat transfer mechanism with spray quenching for 22MnB5 steel." *Appl. Therm. Eng.*, **121**, 48 (2017).